An Efficient Polyphase Filter-Based Resampling Method for Unifying the PRFs in SAR Data

Yoangel Torres, *Student Member, IEEE*, Kamal Premaratne, *Senior Member, IEEE*, Falk Amelung, and Shimon Wdowinski

***Abstract*— Variable higher pulse repetition frequencies (PRFs) are increasingly being used to meet the stricter requirements and complexities of current airborne and spaceborne synthetic aperture radar (SAR) systems associated with higher resolution and wider area products. *POLYPHASE*, the proposed resampling scheme, downsamples and unifies variable PRFs within a single look complex SAR acquisition and across a repeat pass sequence of acquisitions down to an effective lower PRF. A sparsity condition of the received SAR data ensures that the uniformly resampled data approximate the spectral properties of a decimated densely sampled version of the received SAR data. While experiments conducted with both synthetically generated and real airborne SAR data show that POLYPHASE retains comparable performance with the state-of-the-art best linear unbiased interpolation scheme in image quality, a polyphase filter-based implementation of POLYPHASE offers significant computational savings for arbitrary (not necessarily periodic) input PRF variations, thus allowing fully on-board, in-place, and real-time implementation.**

***Index Terms*— Interferometric synthetic aperture radar (InSAR), polyphase filter implementation, synthetic aperture radar (SAR), variable pulse repetition frequency (PRF).**

I. Introduction

SYNTHETIC aperture radar (SAR) and interferometric SAR (InSAR) find application in geophysical and environmental remote sensing applications [1]. However, the complexity of how the data are collected has had to keep pace with advances in sensor technology. Variation in pulse repetition frequency (PRF) is one of these complexities introduced by modern sensors. Methods that make use of displaced phase centers are available to recover the unambiguous Doppler spectrum from nonuniform spatial sampling of the synthetic aperture. A simple two-point interpolation and multichannel reconstruction scheme appears in [2]–[4]. For the single-channel case, [5] provides a frequency-domain algorithm for unambiguous recovery of the Doppler spectrum and [6] has a computationally efficient time-domain scheme that handles nonuniform oversampled SAR data generated from a platform accelerating along-track. However, the method in [6] assumes a constant PRF; the spatial nonuniformity is taken to be solely caused by uncontrolled acceleration of the platform, which is typically much smaller than what could be generated from variable PRFs.

POLYPHASE, the new scheme we propose, tackles nonuniformity along-track within a single look complex (SLC) single-channel or post-beamformed SAR collection arising from different PRFs (or from arbitrary sampling). It takes in demodulated SAR data for different acquisitions, which are collected and oversampled at variable PRFs, and delivers uniformly resampled data within each acquisition at a lower constant PRF in the spatial frequency domain (k-space) [7], [8]. A new polyphase filter-based implementation allows digital filtering at the lowest possible rate, namely, the effective output PRF rate. The result is a computationally efficient fully on-board algorithm enabling in-place and real-time processing, which avoids uplink/downlink data transfers and bottlenecks. The POLYPHSE method approximately reconstructs the collected data on a uniformly spaced grid along the synthetic aperture, while preserving the resolution and Nyquist constraint within the cross-range extent of interest.

We use the spectral properties of the SAR data to justify, and real SAR data to verify, the proposed POLYPHASE scheme. The *best linear unbiased interpolation (BLUI)* scheme in [9] also uses spectral properties to interpolate between nonuniformly oversampled SAR data. However, the type of antenna and the type of noise present may render BLUI suboptimal because of the need to estimate the SNR and numerically evaluate the autocorrelation function of the SAR signal. BLUI also imposes a minimum aperture length (i.e., antenna size) and a maximum platform velocity so that enough number of samples contributes to the interpolation. POLYPHASE simply mandates a lower bound on the sparseness of the received SAR data relative to the output grid. It ensures delivery of uniformly resampled data, which approximates the spectral properties of a decimated version of a 'hidden' densely sampled

Manuscript received February 25, 2017; revised May 10, 2017; accepted June 3, 2017. Date of publication July 3, 2017; date of current version September 25, 2017. This work was supported in part by the University of Miami College of Engineering/RSMAS Collaborative Research Initiative in Environmental Sensing, in part by the U.S. Office of Naval Research under Grant N00014-10-1-0140, and in part by the U.S. National Science Foundation under Grant 1343430. *(Corresponding author: Kamal Premaratne.)*

Y. Torres was with the University of Miami, Coral Gables, FL 33146 USA. He is now with Northrup Grumman Corporation, Melbourne, FL 32901 USA (e-mail: y.torres1@umiami.edu).

K. Premaratne is with the Department of Electrical and Computer Engineering, University of Miami, Coral Gables, FL 33146 USA (e-mail: kamal@miami.edu).

F. Amelung is with the Department of Marine Geosciences, Rosenstiel School of Marine and Atmospheric Science, University of Miami, Coral Gables, FL 33146 USA (e-mail: f.amelung@miami.edu).

S. Wdowinski was with the Rosenstiel School of Marine and Atmospheric Science, University of Miami, Coral Gables, FL 33146 USA. He is now with the Department of Earth and Environment, Florida International University, Miami, FL 33199 USA (e-mail: shimon.wdowinski@fiu.edu).

Color versions of one or more of the figures in this paper are available online at http://ieeexplore.ieee.org.

Digital Object Identifier 10.1109/TGRS.2017.2713600

0196-2892 © 2017 IEEE. Personal use is permitted, but republication/redistribution requires IEEE permission.
See http://www.ieee.org/publications_standards/publications/rights/index.html for more information.

TABLE I
NOTATION

Notation	Description
$\mathbb{C}$, $\mathbb{R}$, $\mathbb{N}$, $\mathbb{N}_+$	Complex numbers, real numbers, integers, and non-negative integers, respectively.
$\mathbb{C}^{M\times N}$, $\mathbb{R}^{M\times N}$	$(M \times N)$-sized matrices with complex- and real-valued entries, respectively.
$(x)_L$	For $x \in \mathbb{R}$, remainder of the dividend $x \in \mathbb{R}$ when $L \in \mathbb{N}_+$ is the divisor.
$\lfloor x \rfloor$, $\lceil x \rceil$	For $x \in \mathbb{R}$, integer value not more than x and integer value not less than x, respectively.
$\delta(n)$, $\delta_D(\omega)$	Kronecker delta function for $n \in \mathbb{N}_+$ and the Dirac delta function for $\omega \in \mathbb{R}$, respectively.
$\int_\theta$	$\int_{\theta=-\pi}^{+\pi}$ unless the limits are explicitly indicated.
c, V_p	Speed of light (m/s) and radar platform velocity (m/s), respectively.
$\lambda_{\min}$, λ_c, $\lambda_{\max}$	Minimum, center, and maximum radar transmit wavelength (m), respectively.
B_{chirp}, PBW	Transmit chirp bandwidth (Hz) and processing Doppler bandwidth (Hz), respectively.
D, D_{pad}	Synthetic aperture length (m) and padded synthetic aperture length (m), respectively.
R, R_0	Slant range between the radar and an arbitrary point on scene (m) and the center of scene (m), respectively.
X_{in}, β, $\Delta\beta$	Cross-rage extent (m), squint angle (rad), and beam sweep angle (rad), respectively.
$\theta_{\min}$, $\theta_{\max}$	Minimum and maximum look angles, respectively, seen by the synthetic aperture (rad).
t, $\overline{f}$, ν	Temporal dimension (s), temporal frequency (Hz), and its rotational counterpart (rad/s) respectively. $\nu = 2\pi\overline{f}$.
u, $\overline{h}$, ω	Spatial dimension (m), spatial frequency (1/m), and its rotational counterpart (rad/m), respectively. $\omega = 2\pi\overline{h}$.
ω_r, ω_{cr}	Wavenumber in range (rad/m) and cross-range (azimuth) (rad/m), respectively. $\omega_r = \nu_r/c$, $\omega_{cr} = \nu_{cr}/V_p$.
δ_r, δ_{cr}	Resolution in range and azimuth, respectively.
K_r, K_{cr}	Broadening factors for pulse weighting in range and aperture weighting in azimuth (or cross-range), respectively.
(x, y, z)	(cross-range, range, height) coordinates of the Cartesian coordinate system (m); scene center is at $(0, 0, 0)$.
$(X_{\text{out}}, Y_{\text{out}})$, (X_n, Y_n, Z_n)	(Azimuth, range) dimensions of the imaged scene (m), Coordinates of the n-th point scatterer within the imaged scene (m).
u, u_k, $u_{\min}$, u_{mid}, $u_{\max}$	Continuous-time x-coordinate, discrete-time x-coordinate, minimum, mid, and maximum x-coordinates, respectively, of the synthetic aperture (m).
Δu_{in}, Δu_{out}	Along-track sample and resample spacings at boresight (m), respectively.
N_{FFT}	Fast Fourier transform (FFT) size used for spatial, or azimuth compression, FFT computation (after zero-padding).
N_{XAC}, N_D, p_d	Number of discrete points needed with and without boundary regions to represent the synthetic aperture length without aliasing and spatial frequency spectrum oversampling factor, respectively. $p_d = (N_{FFT}/N_D)\, K_{cr}$.
PRF_{in}, PRF_{out}	Input and output pulse repetition frequencies, respectively (1/m).
PRI_{in}, PRI_{out}	Input and output pulse repetition intervals, respectively (s). $PRF_{\text{in}} = 1/PRF_{\text{in}}$, $PRF_{\text{out}} = 1/PRF_{\text{out}}$.
γ	Normalized processing bandwidth. $\gamma = PBW/PRF_{\text{out}}$.

SAR data sequence that can be considered to have generated the nonuniformly sampled input SAR data.

Moreover, POLYPHASE works with arbitrary input PRF variations. Thus, it is applicable in more general scenarios (e.g., to compensate for flight path deviation, imaging while in turn, and uncontrolled platform acceleration/deceleration effects [6]). In contrast, BLUI imposes certain periodicity constraints on the input PRF variation to realize its computational savings. In other words, BLUI caters well to the staggered SAR scenario [10], but not for arbitrary PRF variations.

Section II provides a summary of the technical background. Section III provides the main idea, and Sections IV and V more details, of POLYPHASE. Sections VI and VII illustrate the application of POLYPHASE and the ensuing results. Section VIII provides concluding remarks.

II. Technical Background

We use a Cartesian coordinate system with the origin at the scene center, x-axis along-track and parallel to the SAR platform velocity vector V_p (m/s), and y-axis along boresight; z-axis denotes altitude [11]–[14]. Table I shows the notation.

Variable PRFs: While conventional radar system operation relies on a constant PRF, technological advances now allow for newer radar modes of operation, e.g., the high-resolution wide-swath imaging in multichannel SAR allows a shorter revisit time for frequent global mapping. In wide-swath imaging, the antenna length limitation that can restrict the achievable swath width is overcome by a technique based on a single azimuth channel with the system operating with a continuously varied PRF [15]. This allows arbitrary wide swaths and distributes the discrete blind ranges according to the applied PRF span of values. In the end, continuous coverage is achieved at the cost of partial blockage (i.e., loss of some pulses for every target). This PRF variation manifests itself as nonuniform sampling of the slow-time domain along the synthetic aperture [15], thus requiring additional processing, e.g., interpolation schemes to resample the signal to a regular azimuth grid [15].

The advantages offered by high-resolution ultrawide swath SAR imaging is also exploited in multiple elevation beam (MEB) SAR based on variable PRF [16], which employs digital beamforming with a reflector antenna to improve SNR and suppress range ambiguities. It also employs linear variation of the pulse repetition interval (PRI) to overcome the blind range problem of conventional MEB SAR [17].

These new techniques of high-resolution wide-swath imaging modes [15]–[17] come at the cost of nonuniform sampling of the slow-time along-track Doppler phase. Spatial discrete Fourier transform (FT) processing of such nonuniformly spaced data can introduce undesirable artifacts (e.g., smearing, defocusing, and echoing) into the final image (see Fig. 11).

III. Proposed POLYPHASE Resampling Scheme

While the POLYPHASE scheme applies to both strip and spotlight mode SAR, concentrating on the latter, the underlying complex-valued signal of interest $s(\cdot,\cdot)$ is taken as [14]

$$s(\nu_r, u) = S_p(\nu_r) \sum_n \sigma_n e^{-j2\omega_r D_s(n)}. \tag{1}$$

Here, ν_r is the rotational frequency (rad/s) (in range), ω_r is the corresponding wave number (rad/m), $S_p(\nu_r)$ is the

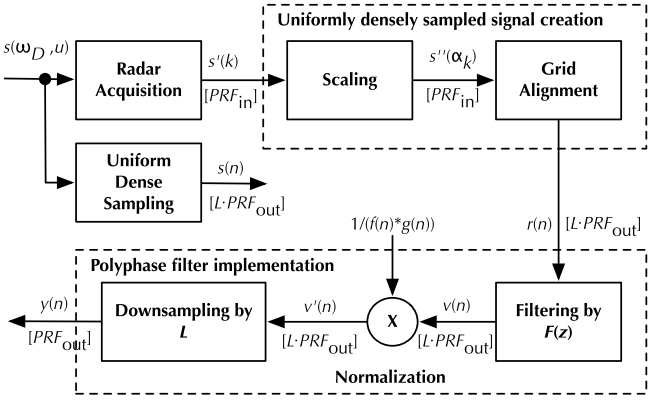

Fig. 1. Block diagram of the proposed POLYPHASE scheme. The sampling rate at each stage is shown within square brackets (e.g., [$\mathrm{PRF_{in}}$]).

discrete-time (DT) FT of the transmitted signal $p(t)$ (in range), σ_n is the reflectivity of the nth scatterer in the scene, $D_s(n) = ((X_n - u)^2 + (Y_n - Y_c)^2 + (Z_n - Z_c)^2)^{1/2}$, (X_n, Y_n, Z_n) are its coordinates, (u, Y_c, Z_c) are the instantaneous radar coordinates, and $u \in [u_{\min}, u_{\max}]$ is the along-track platform position (m). The ground range and altitude coordinates (Y_c, Z_c) are taken to be constants.

A. Uniformly Sampled Radar Signal

Let us uniformly sample the radar signal $s(\nu_r, u)$, $u \in [u_{\min}, u_{\max}]$, where $u_{\min} \le u_0 \le \cdots \le u_{K-1} \le u_{\max}$, with a spatial PRF of $\mathrm{PRF_{in}}$ (1/m). For $k \in \overline{0, K-1}$, this yields the DT signal $s'(\cdot)$ (see Fig. 1), where

$$s'(k) = s(\nu_r, u_k), \quad \text{with } u_{k+1} - u_k = 1/\mathrm{PRF_{in}}. \tag{2}$$

In spotlight mode SAR, unambiguous recovery of the cross-range extent X_{in} at boresight (where $\beta = \pi/2$) requires that the spatial domain PRF satisfy $\mathrm{PRF_{in}} = 1/\Delta u_{\mathrm{in}} \ge \mathrm{PRF_{in,min}} \equiv (2/\lambda_c)\,\Delta\beta = (2/\lambda_c)\,(X_{\mathrm{in}}/R)$, where Δu_{in} and R denote along-track sample spacing (m) and slant range, respectively, $\Delta\beta$ is the beam sweep angle (rad), and $X_{\mathrm{in}} = R\,\Delta\beta$ is the cross-range extent (m) [11], [14]. In spotlight mode SAR, $R\,\Delta\beta$ denotes the maximum cross-range extent illuminated by the radar beam; in strip mode SAR, it is denoted by $X_{\mathrm{in}} = R\,\psi$ where ψ is the real aperture beamwidth.

Fig. 2(a) shows $S_{s'}(\omega_{\mathrm{cr}})$, the frequency response of $s'(\cdot)$ when $\mathrm{PRF_{in}} = \mathrm{PRF_{in,min}}$. In Fig. 2 and onward, we use ω for ω_{cr} [18], [19].

1) A smaller PRF $\mathrm{PRF_{out}} < \mathrm{PRF_{in,min}}$ causes aliasing, and the cross-range extent that can be unambiguously recovered is reduced as $X_{\mathrm{out}} = (\lambda_c/2)\,R\,\mathrm{PRF_{out}} < R\,\Delta\beta$.
2) Uniformly sampling $s(\cdot,\cdot)$ with a higher PRF $L{\cdot}\mathrm{PRF_{out}}$, $L \in \mathbb{N}_+$, where $L{\cdot}\mathrm{PRF_{out}} \gg \mathrm{PRF_{in,min}} = (2/\lambda_c)\,\Delta\beta$, yields $s(\cdot)$, where $s(n) = s(\nu_r, u)|_{u=n/(L\cdot\mathrm{PRF_{out}})}$. Its spectrum $S_s(\omega)$ is in Fig. 2(b).

B. Nonuniformly Sampled Radar Signal

The acquired DT signal $s'(\cdot)$ is a potentially nonuniformly sampled version of $s(\cdot,\cdot)$. The SAR collection receives $s'(\cdot)$ whose variable PRF $\mathrm{PRF_{in}}$ is assumed to be high enough to sample the available Doppler support for an illuminated cross-range extent of $R\,\Delta\beta$ with no aliasing.

1) Model: We view $s'(k) \leftrightarrow S_{s'}(\omega)$ as being the uniformly densely sampled signal $s(n) \leftrightarrow S_s(\omega)$ but with 'missing' samples. Here, $\leftrightarrow$ denotes a DT FT pair (in the deterministic case) or a PSD (power spectral density) pair (in the stochastic case). Then, with appropriate scaling and grid alignment, the signal $r(n) \leftrightarrow S_r(\omega)$ in Fig. 1 can be viewed as a 'gated' version of $s(n)$, i.e., $r(n) = g(n)\,s(n)$, where the gating function $g(n) \leftrightarrow S_g(\omega)$ is a realization of an independent identically distributed (i.i.d.) Bernoulli random process with parameter p. Thus, the probabilities of $g(n)$ taking the values 1 and 0 are given by

$$\Pr(g(n) = 1) = p; \;\; \Pr(g(n) = 0) = 1 - p \quad \forall\, \mathbb{N} \tag{3}$$

respectively. Using $S_x(\omega)$ to denote the PSD of the w.s.s. random process $x(\cdot)$, we get the PSD of $g(n)$ as

$$S_g(\omega) = p(1-p) + (2\pi p^2) \sum_{k=-\infty}^{+\infty} \delta_D(\omega - 2\pi k). \tag{4}$$

Since the PSD of $r(n)$ is given by $S_r(\omega) = (1/2\pi)\,(S_g(\omega) * S_s(\omega))$, we get $S_r(\omega)$ as a scaled 'biased' version of $S_s(\omega)$

$$S_r(\omega) = \frac{1}{2\pi}\, p(1-p) \int_{\omega} S_s(\omega)\, d\omega + p^2 S_s(\omega). \tag{5}$$

2) Spatial Doppler Bandwidth Recovery at Output PRF: Suppose we are interested in an image signal from which a cross-range extent of X_{out} can be recovered with a sampling rate of $\mathrm{PRF_{out}}$ (1/m). As we show in Appendix A, such a signal, which approximates a downsampled version of $s(n)$ (which is at the constant PRF $L{\cdot}\mathrm{PRF_{out}}$), can be generated from the resampling scheme in Fig. 1 by implementing the following three operations.

1) Get $v(n)$ by filtering $r(n)$ by a digital filter $f(n) \leftrightarrow F(z)$ with the magnitude response

$$|F(\omega)| = 1,\ |\omega| \le \gamma\,\pi/L; \quad |F(\omega)| = 0, \quad \pi/L \le |\omega|, \tag{6}$$

where $L \gg 1$.
2) Normalize $v(n)$ by $f(n) * g(n)$ to get $v'(n)$.
3) L-fold decimate $v'(n)$ to get $y(n)$.

Then, if $p \gg \rho/(L+\rho)$, where $\rho = \mathrm{PRF_{in}}/\mathrm{PRF_{out}} \ge 1$, the PSD of the output $y(n)$ approximates the PSD of an L-fold decimated version of the uniformly densely sampled signal $s(n)$ within the frequency band $[0, \gamma\,\pi]$. Thus, to recover a spatial Doppler bandwidth of PBW (Hz) corresponding to N_{save} bins, we must have $\gamma = N_{\mathrm{save}}/N_{\mathrm{FFT}}$ (or equivalently, $\gamma = \mathrm{PBW}/\mathrm{PRF_{out}}$). Note that N_{save} is the number of bins guaranteed to be retained in the final image without distortion.

IV. Output Grid Spacing Design

Here we select the slow-time output grid spacing Δu_{out} (m) so that it conforms to a given spatial PRF $\mathrm{PRF_{out}}$, preserves the resolution in the image domain, and avoids aliasing in both spatial slow-time and image domains. The output grid

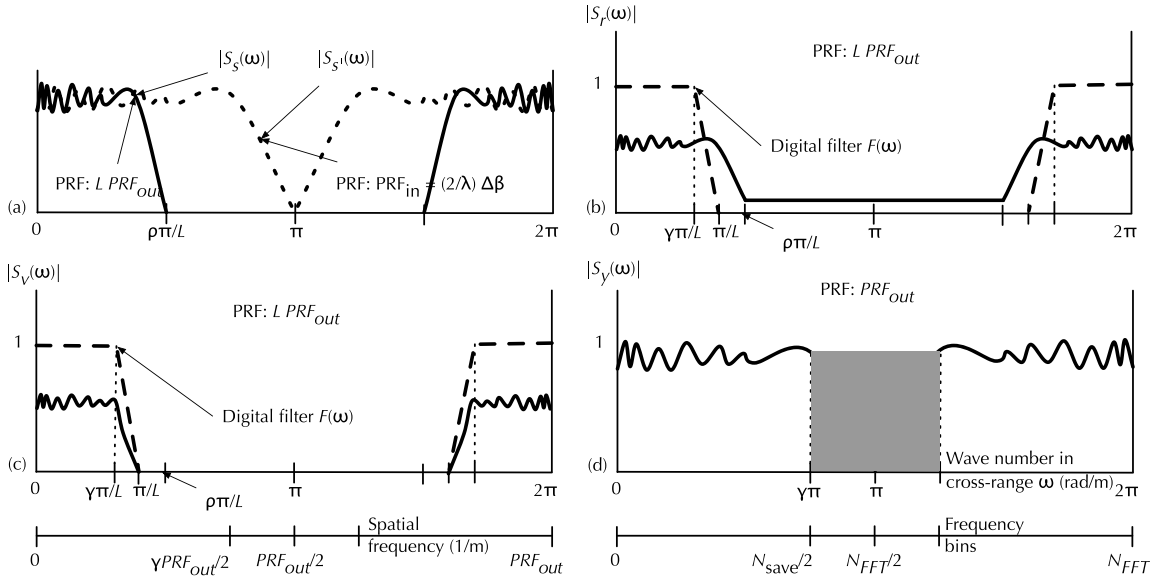

Fig. 2. Spatial Doppler bandwidths. (a) Dotted line is $s'(k)$ at a PRF of $\mathrm{PRF_{in}} = \mathrm{PRF_{in,min}} = (2/\lambda_c)\,\Delta\beta$ (1/m) and solid line is $s(n)$ at a PRF of $L{\cdot}\mathrm{PRF_{out}}$ (1/m). (b) $r(k)$ at a PRF of $L{\cdot}\mathrm{PRF_{out}}$ (1/m). (c) $v(k)$ at a PRF of $L{\cdot}\mathrm{PRF_{out}}$ (1/m). (d) $y(k)$ at a PRF of $\mathrm{PRF_{out}}$ (1/m). The digital filter $F(z)$ has its passband and stopband edges at $\gamma\pi/L$, $\gamma < 1$, and π/L, respectively, $\rho = \mathrm{PRF_{in}}/\mathrm{PRF_{out}} \geq 1$, N_{save} denotes the number of bins guaranteed to be retained in the final image without distortion, and $\gamma = N_{\mathrm{save}}/N_{\mathrm{FFT}} = \mathrm{PBW}/\mathrm{PRF_{out}} < 1$. Spatial frequency value (with respect to the PRF $\mathrm{PRF_{out}}$) and frequency bin axes are also shown underneath (c) and (d).

spacing $\Delta u_{\mathrm{out}}/L$ is then used to view the raw data $s'(k)$ (at the variable PRF $\mathrm{PRF_{in}}$) as being embedded in a uniformly densely sampled signal $r(n)$ (at the constant PRF $L{\cdot}\mathrm{PRF_{out}}$).

A. Design Steps

1) FFT Size: Following common practice, we first select the azimuth compression FFT size N_{FFT} to meet the read access memory and SAR processor power/speed limitations.

2) Synthetic Aperture: Note that N_{FFT} is the next power-of-two FFT size obtained from N_D, the number of points necessary to represent the synthetic aperture with no aliasing. Then, the slow-time spectrum oversampling factor is

$$p_d = K_{\mathrm{cr}}\,(N_{\mathrm{FFT}}\,\Delta u_{\mathrm{out}})/(N_D\,\Delta u_{\mathrm{out}}) = K_{\mathrm{cr}}\,N_{\mathrm{FFT}}/N_D \quad (7)$$

where K_{cr} compensates for broadening due to aperture weighting [13]. Note that $N_D\,\Delta u_{\mathrm{out}}$ and $N_{\mathrm{FFT}}\,\Delta u_{\mathrm{out}}$ denote the slow-time acquisition intervals D and D_{pad} generated by N_D and N_{FFT}, respectively. Thus, $K_{\mathrm{cr}} \leq p_d$ because $N_D \leq N_{\mathrm{FFT}}$. We used $p_d = 1.5$ to generate adequate oversampling for a visually more pleasing image and to facilitate application of certain image processing procedures. Then (7) yields N_D.

Filtering by the order N_{pr} prototype $H_{\mathrm{pr}}(z)$ (see Section V-A) requires N_{pr} number of samples to be appended to the N_D number of points laid out along the synthetic aperture. This yields a total of $N_{XAC} = N_D + N_{\mathrm{pr}}$ number of points.

3) Slow-Time Output Grid Spacing and Output: We match range and azimuth resolutions to get square radar resolution cells in the oversampled image domain. Equating the range and azimuth resolution expressions in spotlight mode SAR $\delta_r = (c/2)\,(K_r/B_{\mathrm{chirp}})$ and $\delta_{\mathrm{cr}} = (\lambda_c/2)\,(K_{\mathrm{cr}}/\Delta\beta)$ [11]–[13], we get the SAR integration angle $\Delta\beta = (\lambda_c B_{\mathrm{chirp}}/c)\,(K_{\mathrm{cr}}/K_r)$, which yields the required synthetic aperture length D [14]. The slow-time output grid spacing Δu_{out} and the corresponding spatial sampling frequency $\mathrm{PRF_{out}}$ of the resampled data are then given by $\Delta u_{\mathrm{out}} = D/N_D$ so that $\mathrm{PRF_{out}} = 1/\Delta u_{\mathrm{out}}$.

4) Cross-Range Extent: With $X_{\mathrm{out}} = (\lambda_c/2)\,R\,\mathrm{PRF_{out}}$, and for the selected FFT size N_{FFT}, we are attempting to fit as much cross-range extent X_{out} as possible so that PRF conversion is more efficient: it is more parallel processing friendly, and aid the SAR processor to partition the image into smaller patches of cross-range extent allowing smaller FFT sizes to be run faster on parallel nodes.

B. Grid Alignment

1) Scaling: We use $s(\nu_r, \alpha) = s(\nu_r, u)|_{u=\Phi^{-1}(\alpha)}$, where $\alpha = \Phi(u) = (u - u_{\mathrm{mid}})/\Delta u_{\mathrm{out}} + (N_D + 1)/2$, to linearly transform the input to the output spatial grid. Here, $u \in [u_{\min}, u_{\max}]$, $\Delta u_{\mathrm{out}} = (u_{\max} - u_{\min})/N_{XAC}$ is the output spacing along-track, and $N_D = N_{XAC} - N_{\mathrm{pr}}$ is the number of output points along the acquisition interval D. With $\alpha_k = \Phi(u_k)$, $k \in \overline{0, K}$, this transforms the sequence $s'(\cdot)$ to the sequence $s''(\cdot)$, where $s''(k) \equiv s(\nu_r, \alpha_k) = s(\nu_r, u_k) \equiv s'(k)$.

2) Grid Alignment: Next we align $s''(\cdot)$ onto a dense grid corresponding to the rate $L{\cdot}\mathrm{PRF_{out}}$ to create $r(\cdot)$, where

$$r(n) = s''(\alpha_k), \quad \text{for } n = \lfloor L \cdot \alpha_k \rfloor \quad (8)$$

and $r(n) = 0$ otherwise. Here, $\lfloor x/L \rfloor = (x - (x)_L)/L$, where $(x)_L$ denotes the remainder when x and L are the dividend and divisor, respectively. Each sampled value in $s''(k)$ is now aligned to a grid point within the densely sampled grid with rate $L{\cdot}\mathrm{PRF_{out}}$. The remaining grid points (i.e., the 'missing' samples) have value 0. Thus, $r(\cdot)$ can be viewed as a 'gated'

version of $s(\cdot)$, where only some samples of $s(\cdot)$ appear in $r(\cdot)$ (see Section III-B and Appendix A).

V. Filter Design and Implementation

A flexible SAR focusing processor (i.e., TerraSAR-X) must accommodate a wide range of integer and noninteger resample ratios (which can vary with radar collection parameters, geometry, processed image resolution and scene size, FFT size, etc.). Thus, POLYPHASE's narrowband digital filter [see (6)] must be flexible enough to handle a large range of resampling ratios and it must be efficiently implemented. A polyphase implementation architecture, a critical component in multirate digital systems [19], addresses both these issues.

A. Filter Design

Step 1 Prototype Filter: Use a standard finite impulse response (FIR) filter design technique (see [18]) to design a 'prototype' $F_{\rm pr}(z) = \sum_{m=0}^{N_{\rm pr}} f_{\rm pr}(m)\, z^{-m}$ with passband and stopband edge frequencies 'stretched' L-times as those in (6)

$$F_{\rm pr}(\omega) = 1,\ \omega \in [0, \gamma\, \pi]; \quad F_{\rm pr}(\omega) = 0,\ \omega = \pi. \tag{9}$$

We choose a Type-II FIR filter design (with symmetric filter taps and odd filter order $N_{\rm pr}$). One may also use a Type-I FIR filter (with symmetric filter taps and even filter order).

Step 2 Shaping Filter: As is typical in interpolated FIR (IFIR) filter design [20], [21], generate an L-fold upsampled version of $f_{\rm pr}(n)$ to get the 'shaping' filter

$$f_{\rm be}(n) = \begin{cases} f_{\rm pr}(n/L), & \text{for } n = 0, L, \ldots, N_{\rm pr} L \\ 0, & \text{otherwise} \end{cases} \tag{10}$$

so that $F_{\rm be}(z) = F_{\rm pr}(z^L)$. This $N_{\rm pr} L$-order filter's frequency response is the desired response in (6), except that spectral 'images' of this desired response now appear within the Nyquist interval. The filter order $N_{\rm pr} L$ enables a polyphase design consisting of L subfilters [18].

Step 3 *Image Suppression:* IFIR designs require a 'masking' filter to suppress these extra images [21]. But, this increases the length of our overall impulse response (IPR) and the filter order beyond $N_{\rm pr} L$. Thus, we employ a direct least squared integral error (LSIE) FIR design [22], [23] to design an $N_{\rm pr} L$-order filter to approximate $F_{\rm be}(\omega)$ in the frequency interval $[0, \pi/L]$. Then, the 'ideal' frequency response to be approximated is $F_{\rm id}(\omega) = F_{\rm be}(\omega)\, F_{\rm LPF}(\omega)$, where

$$F_{\rm LPF}(\omega) = 1,\ |\omega| \le \pi/L;\ F_{\rm LPF}(\omega) = 0, \quad \text{otherwise}. \tag{11}$$

Note that $F_{\rm LPF}(\omega) \leftrightarrow f_{\rm LPF}(n) = (1/L)\,\mathrm{sinc}(\pi n/L)$ and $f_{\rm id}(n) = f_{\rm be}(n) * f_{\rm LPF}(n)$. Thus

$$f_{\rm id}(n) = \frac{1}{L} \sum_{m=0}^{N_{\rm pr}} f_{\rm pr}(m)\, \mathrm{sinc}\left((n - mL)\frac{\pi}{L}\right) \tag{12}$$

and the filter with support in $[0, N_{\rm pr} L]$ that minimizes the LSIE with $F_{\rm id}(\omega)$ is [22], [23]

$$f(n) = \frac{1}{L} \sum_{m=0}^{N_{\rm pr}} f_{\rm pr}(m)\, \mathrm{sinc}\left((n - mL)\frac{\pi}{L}\right). \tag{13}$$

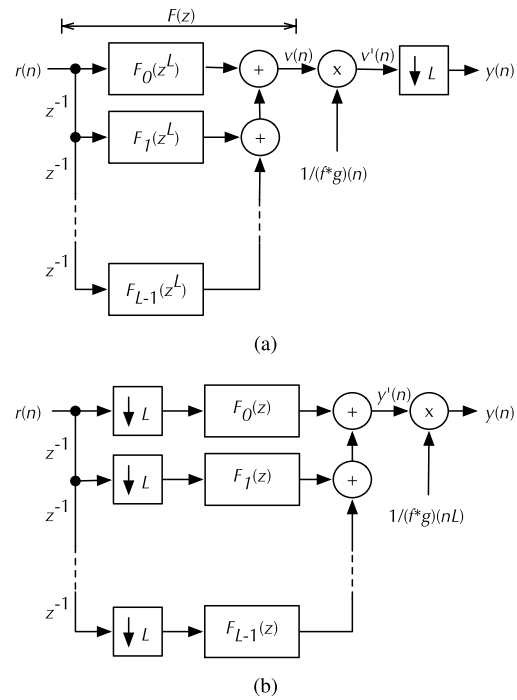

Fig. 3. Efficient polyphase implementation of the filter $F(z)$. The structure in (b) allows the digital filtering operations in (a) to be carried out at the lowest sampling rate. (a) Polyphase representation of F(z). (b) Efficient implementation of (a).

B. Polyphase Filter Implementation

Consider the L-fold polyphase representation of $F(z)$ [18]

$$F(z) = \sum_{\ell=0}^{L-1} z^{-\ell} F_\ell(z^L), \quad \text{with } F_\ell(z) = \sum_{n=0}^{N_{\rm pr}} f_\ell(n)\, z^{-n}. \tag{14}$$

Here, $f_\ell(n) = f(nL + \ell)$ [see Fig. 3(a)]. Note that $F_0(z)$ is of order $N_{\rm pr}$ and $F_\ell(z)$, $\ell \in \overline{1, L-1}$, is of order $N_{\rm pr} - 1$.

To create the final output $y(n)$, we normalize the filtered output $v(n)$ to get $v'(n) = v(n)/(f(n) * g(n))|_{nL}$, and L-fold downsample $v'(n)$ [see Figs. 1 and 3(a)]. As is well known [19], the alternate implementation of the structure in Fig. 3(a) that appears in Fig. 3(b) allows the filtering operations to be performed at the lowest sampling rate.

1) Normalization: In Fig. 3(a), the normalized output $v'(n)$ must be downsampled to produce the required output $y(n)$. In the more efficient implementation of Fig. 3(b), normalization immediately produces $y(n)$. This 'normalized' convolution may be interpreted as associating a level of 'confidence' with the received signal [24]–[26]. For example, each missing sample is associated with zero confidence. Accordingly, $f(n) * g(n)$, where the gating function $g(n)$ (see Section III-B) captures the confidence associated with the received signal $r(\cdot)$. The normalization factor $(f(n) * g(n))|_{nL}$ is computed by maintaining a separate buffer, which accumulates the sum of the coefficients used at each output location.

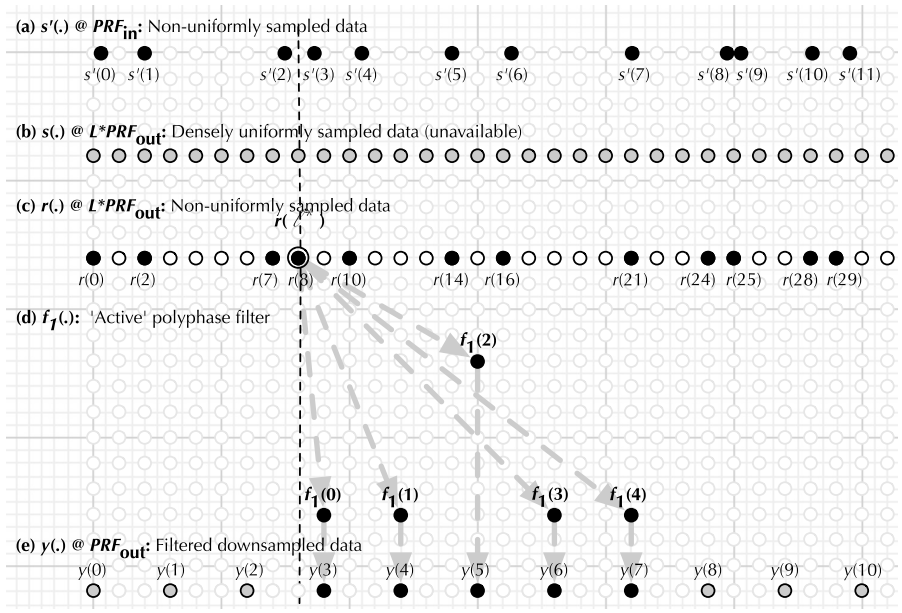

Fig. 4. Implementation of POLYPHASE with $N_{\text{pr}} = 5$ and $L = 3$ (see Figs. 1 and 3). The only polyphase component that operates on the input sample $r(\ell^*) = r(8)$ is $f_1(n) \leftrightarrow F_1(z)$ that is of order $N_{\text{pr}} - 1 = 4$ and has $N_{\text{pr}} = 5$ taps. The filtered outputs $f_1(n-3)\,r(\ell^*)$, $n \in \overline{3,7}$, are used to update the output sample $y(n)$.

2) Generating the Output: With $n_{\text{pr}} = n - N_{\text{pr}}$, the output $y(n) = y'(n)/(f(n) * g(n))|_{nL}$ can be expressed as

$$y'(n) = f_0(N_{\text{pr}})\,r(n_{\text{pr}}L) + \sum_{m=n_{\text{pr}}+1}^{n} \sum_{\ell=mL-(L-1)}^{mL} f_{mL-\ell}(n-m)\,r(\ell). \quad (15)$$

Thus, computation of one output sample $y'(n)$ requires all nonzero input samples $r(\ell)$ such that $(n - N_{\text{pr}})L \leq \ell \leq nL$. Conversely, the single nonzero input sample $r(\ell)$ affects the computation of all output samples $y(n)$ such that $\ell \leq nL \leq \ell + N_{\text{pr}}L$

$$y(n) \text{ s.t. } \left\lfloor \frac{\ell - 1}{L} \right\rfloor + 1 \leq n \leq \left\lfloor \frac{\ell}{L} \right\rfloor + N_{\text{pr}}. \quad (16)$$

Note that, with the polyphase implementation, a given nonzero input sample $r(\ell^*)$ such that $(n - N_{\text{pr}})L \leq \ell^* \leq nL$ is operated on by only one polyphase component $f_x(\cdot)$, where $x = m^*L - \ell^*$ with $m^* = \lfloor(\ell^* - 1)/L\rfloor + 1$ (see Claim 2 in Appendix B).

3) Summary: We use Fig. 4 to explain the above operations.

1) *Black* circles denote $s'(\cdot)$ [see (2)].
2) *Gray* circles denote $s(\cdot)$, the signal that is densely uniformly sampled at a rate of $L\,\text{PRF}_{\text{in}}$ (see Section III-A). Note that $s(\cdot)$ is unavailable, and the input $s'(\cdot)$ is viewed as being generated from $s(\cdot)$, but with a high (approximately $1 - p$) fraction of $s(\cdot)$'s samples missing [see (3)].
3) *Black* circles denote $r(\cdot)$, which is the input $s'(\cdot)$ aligned to the same 'sampling grid' as $s(\cdot)$ [see (8)]. To explain, let $N_{\text{pr}} = 5$ and $L = 3$ (our actual implementation uses $L = 64$). Thus, the order of the narrowband digital filter $F(z)$ is $N_{\text{pr}}L = 15$ and it has $L = 3$ polyphase components $\{F_0(z), F_1(z), F_2(z)\}$: $F_0(z)$ is of order $N_{\text{pr}} = 5$; $F_1(z)$ and $F_2(z)$ are each of order $N_{\text{pr}} - 1 = 4$ [see (6), (9), and (14)].
4) *Ringed black* circle identifies one nonzero input sample $r(\ell^*)$, $\ell^* = 8$. With $L = 3$, the range of ℓ in the second summation in (15) is $3m \leq \ell \leq 3m - 2$. In this range, $\ell = \ell^* = 8$ occurs only when $m^* = 3$. In turn, from the first summation in (15), the only values of n that would require $r(\ell^*) = r(8)$ must satisfy $3 \leq n \leq 7$ [see (16)]. Thus, when the input sample $r(\ell^*) = r(8)$ is received, we must update the output samples $y'(n)$, $3 \leq n \leq 7$, by $f_{3m^*-\ell^*}(n - m^*)\,r(\ell^*) = f_1(n-3)\,r(8)$.
5) $\ell^* = 8$ implies $m^* = 3$. Thus, *only* $f_{3m^*-\ell^*}(\cdot) = f_1(\cdot)$ polyphase component is activated (Claim 2 in Appendix B). *Black* circles indicate the $N_{\text{pr}} = 5$ taps of the filter $f_1(n) \leftrightarrow F_1(z)$. The *gray* arrows show output samples being updated by these taps operating on $r(\ell^*)$.
6) *Black* circles denote $y(\cdot)$, $3 \leq n \leq 7$, the output samples that get updated with the input sample $r(\ell^*) = r(8)$. This updating is carried out 'on-the-fly' with no input buffering.

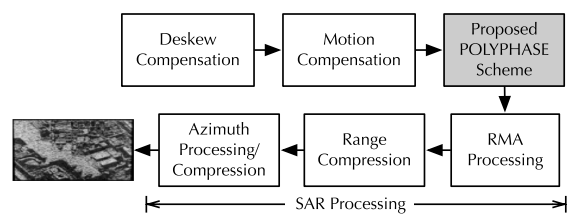

Fig. 5. Proposed POLYPHASE scheme's role within the image formation process.

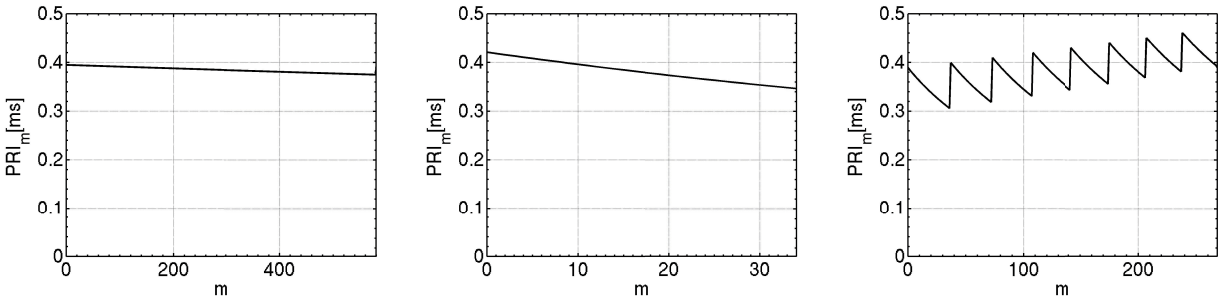

Fig. 6. One period of the PRI variations. Each variation has mean PRI $\mathrm{PRI}_{\mathrm{mean}} = 0.385$ ms, minimum range of swath $R_{0_{\mathrm{min}}} = 837$ km, maximum range of swath $R_{0_{\mathrm{max}}} = 1047$ km, and pulsewidth 15 μs [9]. (a) Slow PRI variation with $\mathrm{PRI}_{\mathrm{max}} = 0.395$ ms, $\mathrm{PRI}_{\mathrm{min}} = 0.375$ ms, and period 580 m. (b) Fast PRI variation with $\mathrm{PRI}_{\mathrm{max}} = 0.421$ ms, $\mathrm{PRI}_{\mathrm{min}} = 0.349$ ms, and period 34 m. (c) Elaborate PRI variation with $\mathrm{PRI}_{\mathrm{max}} = 0.461$ ms, $\mathrm{PRI}_{\mathrm{min}} = 0.309$ ms, and period 268 m.

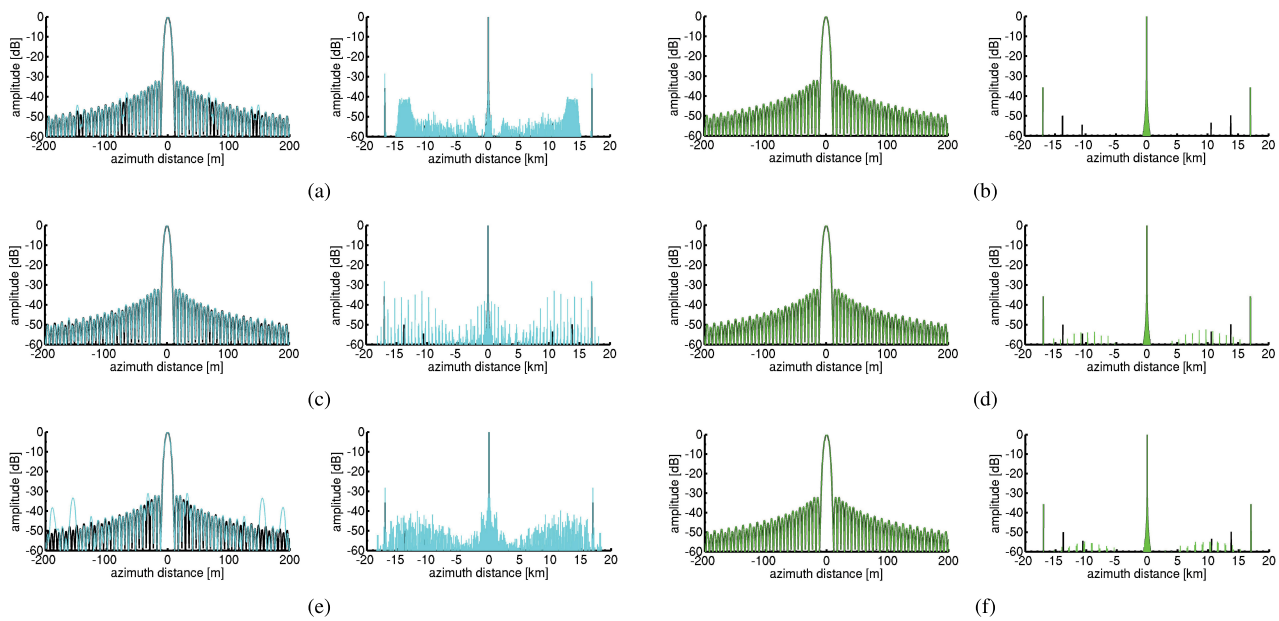

Fig. 7. Scenario I (scatterers at $\{0, \pm 17\}$ km): comparison of BLUI and POLYPHASE using the azimuth IPRs corresponding to the three different PRI variations in Fig. 6. Each IPR is depicted over 400 m and 40 km azimuth scales. The underlying black curves represent the reference IPR of a SAR system with a constant PRI equal to the mean PRI $\mathrm{PRI}_{\mathrm{mean}} = 0.385$ ms. (a) BLUI with slow PRI variation. (b) POLYPHASE with slow PRI variation. (c) BLUI with fast PRI variation. (d) POLYPHASE with fast PRI variation. (e) BLUI with elaborate PRI variation. (f) POLYPHASE with elaborate PRI variation.

7) *Gray* circles denote the full set of output samples that need to be computed. Its PSD approximates the PSD of an L-fold decimated ($L = 3$) version of $s(n)$ within the frequency band $[0, \gamma\, \pi]$ (Claim 1 in Appendix A).

Fig. 5 shows where the proposed scheme belongs within the image formation process.

VI. Results

A. Synthetic Data

To see how the azimuth IPR is affected by the different PRI variations in [9], namely, the slow, the fast, and the elaborate PRI variations in Fig. 6, two different scenarios, each containing three scatterers and covering a total unambiguous azimuth extent of 40 km, are considered. We used a slant range of $R = 1000$ km, an orbit height of 760 km, a wavelength of $\lambda = 0.2384$ m (L-band), and a planar antenna of length of 7 m. The azimuth processed bandwidth is set to PBW = 800 Hz. In addition, an azimuth Hamming window ($\alpha = 0.6$) and a window which compensates for the azimuth antenna pattern are employed to arrive at an azimuth resolution of 7 m. The output PRI for all simulations is $\mathrm{PRI}_{\mathrm{out}} = 0.417$ ms.

1) Scenario I With Scatterers at $\{0, \pm 17\}$ *km:* Fig. 7 shows the azimuth IPRs generated by BLUI and POLYPHASE for the three periodic PRI variations in Fig. 6 with scatterers at $\{0, \pm 17\}$ km. The underlying black curves represent the reference IPR of a SAR system with a constant PRI equal to the mean PRI $\mathrm{PRI}_{\mathrm{mean}} = 0.385$ ms.

2) Scenario II With Scatterers at $\{0, \pm 175\}$ *m:* Fig. 8 shows the azimuth IPRs generated by BLUI and POLYPHASE for the three periodic PRI variations in Fig. 6 with scatterers at $\{0, \pm 175\}$ m. The underlying black curves represent the

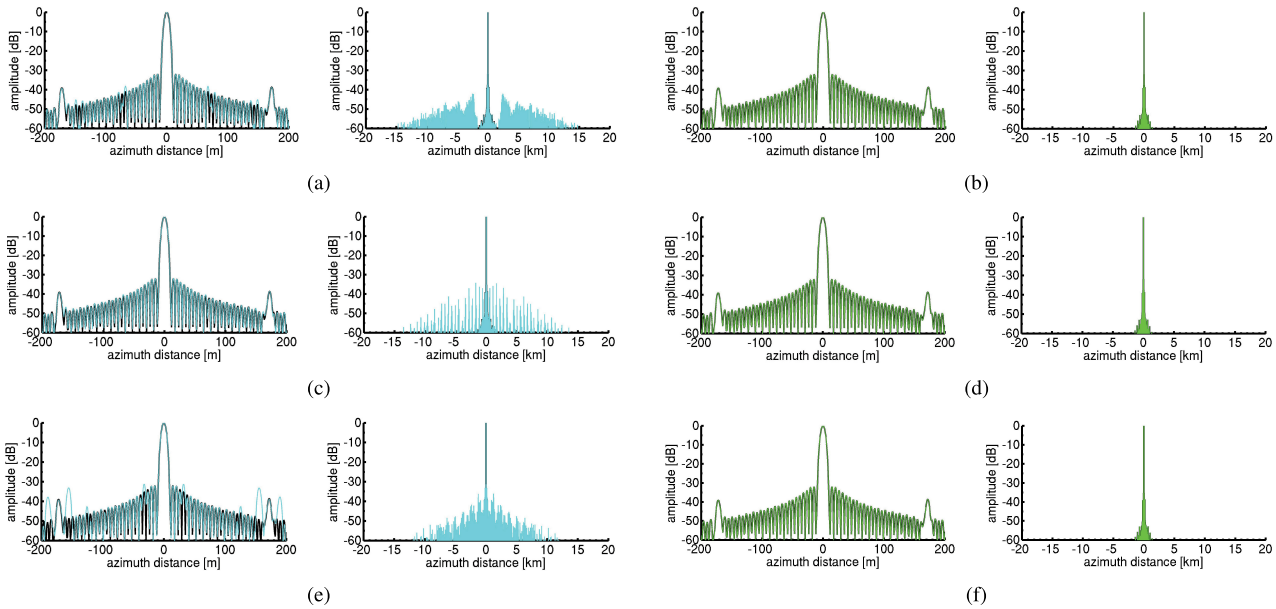

Fig. 8. Scenario II (scatterers at $\{0, \pm 175\}$ m): comparison of BLUI and POLYPHASE using the azimuth IPRs corresponding to the three different PRI variations in Fig. 6. Each IPR is depicted over 400 m and 40 km azimuth scales. The underlying black curves represent the reference IPR of a SAR system with a constant PRI equal to the mean PRI $\text{PRI}_{\text{mean}} = 0.385$ ms. (a) BLUI with slow PRI variation. (b) POLYPHASE with slow PRI variation. (c) BLUI with fast PRI variation. (d) POLYPHASE with fast PRI variation. (e) BLUI with elaborate PRI variation. (f) POLYPHASE with elaborate PRI variation.

TABLE II

ISLR AND PSLR FOR THE IPRS IN FIGS. 7 AND 8 FOR SCENARIOS I AND II

	PRI Variation	Reference I	Reference II	BLUI I	BLUI II	POLYPHASE I	POLYPHASE II
ISLR (dB):	**Slow**	-18.30	-18.27	-17.98	-17.94	-18.30	-18.27
	Fast	-18.30	-18.27	-18.23	-18.17	-18.30	-18.27
	Elaborate	-18.30	-18.27	-17.62	-17.66	-18.30	-18.27
PSLR (dB):	**Slow**	-32.11	-31.93	-32.04	-31.84	-32.11	-31.93
	Fast	-32.11	-31.93	-32.01	-31.89	-32.11	-31.93
	Elaborate	-32.11	-31.93	-31.10	-31.29	-32.09	-31.93

reference IPR of a SAR system with a constant PRI equal to the mean PRI $\text{PRI}_{\text{mean}} = 0.385$ ms.

These, and Table II that compares the two schemes relative to the response of a constant PRI, show that POLYPHASE achieves nearly perfect reconstruction.

B. Real Data

1) Data Sets: We employ data set A and data set B that had been acquired with stretch waveforms (using the "deramp-on-receive" technique) in SAR's spotlight mode, with the PRI slaved to a primary mode possessing the nonuniform PRI variations in Fig. 9(a) and (b), respectively. The acquisition and processing parameters are in Table III. The azimuth processed bandwidth is set to $\text{PBW} \approx (2/3)\text{PRF}_{\text{out}}$ [i.e., $N_{\text{save}} = (2/3)\, N_{\text{FFT}}$]. An azimuth Taylor window (with $\bar{n} = 6$ and sidelobe $= -35$ dB) was used to get an azimuth resolution of 0.75 m per resolution cell [12]. The azimuth antenna pattern was not compensated for because the antenna pattern as seen by a target is constant in spotlight mode [27].

2) Results: Fig. 10(a) shows the frequency responses of the high-order narrowband digital filter $F(z)$ [in (6)] and the

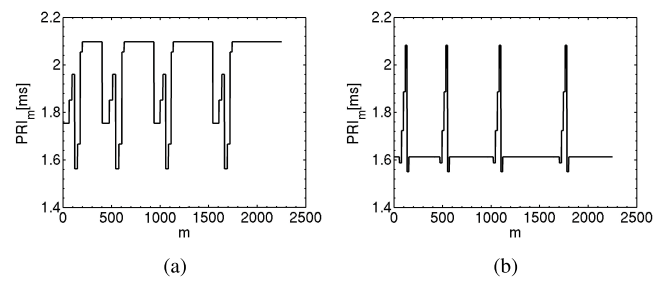

Fig. 9. Periodic PRI sequences associated with data set A and data set B. The pulsewidth is 66.7 μs. (a) Data set A: $\text{PRI}_{\text{mean}} = 1.984$ ms, $\text{PRI}_{\text{max}} = 2.098$ ms, $\text{PRI}_{\text{min}} = 1.562$ ms, and $R_0 = 135$ km. (b) Data set B: $\text{PRI}_{\text{mean}} = 1.637$ ms, $\text{PRI}_{\text{max}} = 2.083$ ms, $\text{PRI}_{\text{min}} = 1.550$ ms, and $R_0 = 118$ km.

TABLE III

ACQUISITION AND PROCESSING PARAMETERS CORRESPONDING TO DATA SETS A AND B

Common Acquisition Parameters: $B_{chirp} = 240$ (MHz); $\Delta\beta = 1.6$ (deg); $\lambda_c = 0.031$ (m); platform height $= 12.8$ (km); planar antenna length $= 1.45$ (m).
Common Processing Parameters: $K_{cr} = 1.2$; $L = 64$; $N_{FFT} = 16384$; $p_d = 1.5$; $Y_{\text{out}} = 3360$ (m).

Data-set	D (m)	R_0 (m)	$R\Delta\beta$ (m)	β (deg)	V_p (m/s)	PBW (Hz)	PRF_{out} (Hz)	X_{out} (m)
A	3395.29	118320	3304.12	13.8	142.68	367	551	7086.94
B	3821.59	135205	3762.85	10.75	136.59	312	468	7196.15

shaping filter $F_{\text{be}}(z)$ [in (10)]; Fig. 10(b) shows the low-order subfilter $F_0(z)$ [in (14)].

Fig. 11 shows the results. Fig. 11(a) and (c) refers to data set A: Fig. 11(a) shows the image formed with the spatial FT taken on data nonuniformly sampled along-track, i.e., the resampler block in Fig. 5 is absent; Fig. 11(c) shows the image formed after taking the discrete spatial FT on data that

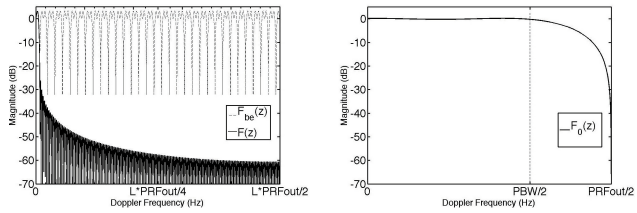

(a) (b)

Fig. 10. Digital filter frequency responses. (a) Narrowband digital filter $F(z)$ [in (6)] and the shaping filter $F_{\mathrm{be}}(z)$ [in (10)] both of order $N_{\mathrm{pr}}L = (5)(64) = 320$. (b) Polyphase subfilter $F_0(z)$ [in (14)] of order $N_{\mathrm{pr}} = 5$.

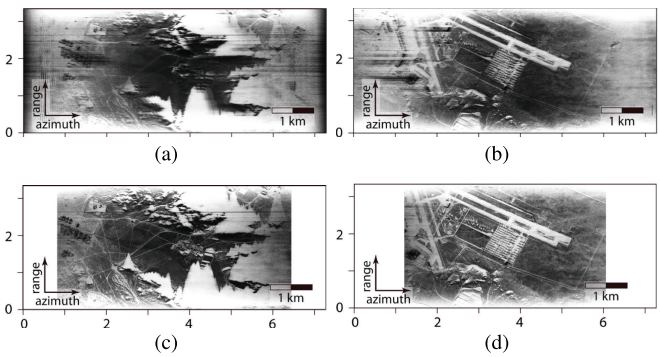

(a) (b) (c) (d)

Fig. 11. Application of POLYPHASE to data sets A and B. (a) Data set A: nonuniformly sampled along-track formed image. (b) Data set B: nonuniformly sampled along-track formed image. (c) Data set A: uniformly resampled along-track formed and passband cropped image. (d) Data set B: uniformly resampled along-track formed and passband cropped image.

TABLE IV

PERFORMANCE COMPARISON OF BLUI AND POLYPHASE

Original (Non-Uniformly Sampled Data)		BLUI		POLYPHASE	
Dataset A	**Dataset B**	**Dataset A**	**Dataset B**	**Dataset A**	**Dataset B**
ISLR (dB):					
−2.39	1.09	−10.12	−1.95	−10.15	−2.00
PSLR (dB):					
−2.0	−2.2	−21.0	−9.2	−21.1	−9.3
IPR (m): (8 scatterers)					
1.51, 1.64	1.48, 1.52	0.87, 0.86	0.90, 0.93	0.86, 0.84	0.88, 0.92
1.78, 1.89	1.45, 1.31	1.07, 1.21	0.82, 0.84	1.05, 1.20	0.82, 0.83
0.92, 0.98	1.23, 0.88	0.75, 0.75	0.78, 0.73	0.72, 0.74	0.76, 0.72
0.89, 0.82	0.91, 0.85	0.73, 0.72	0.75, 0.73	0.73, 0.71	0.74, 0.73

have undergone the resampling system in the spatial slow-time domain, i.e., the resampler block in Fig. 5 is operational. Similarly, Fig. 11(b) and (d) refers to data set B: Fig. 11(b) shows the image formed with the spatial FT taken on data nonuniformly sampled along-track; Fig. 11(d) shows the image formed after taking the discrete spatial FT on data that have undergone the resampling system in the spatial slow-time domain. In Fig. 11(c) and (d), images have been cropped in azimuth to the processing bandwidth $\mathrm{PBW} = (2/3)\,\mathrm{PRF}_{\mathrm{out}}$ [or, $N_{\mathrm{save}} = (2/3)\,N_{\mathrm{FFT}}$ pixels].

Table IV compares the integrated side lobe ratio (ISLR) and peak side lobe ratio (PSLR) measurements (relative to the original nonuniformly sampled data).

3) Resolution Improvement: To quantify the improvement in resolution offered by POLYPHASE, we used IPR to measure how resolvable point scatterers are in azimuth [28]. In particular, we employed a quadratic fit of the log magnitude of pixels adjacent to the peak of the main lobe response of point scatterers, and then recorded the −3 dB width as an indication of resolution. Table IV indicates the average improvement corresponding to eight point scatterers.

VII. DISCUSSION

A. Computational Complexity

As commonly practiced, we used the number of *flops* (i.e., the number of real additions and multiplications) [29], [30] to compare the computational burdens. Note that BLUI is *output-based* (i.e., it takes in a vector of input samples to compute an output sample); POLYPHASE is *input-based* (i.e., it takes an input sample and updates a vector of output samples).

POLYPHASE. Each complex-valued input sample $r(n) \in \mathbb{C}$ goes through N_{pr} real-valued taps of one polyphase component to update N_{pr} output samples (see Fig. 4), entailing $4N_{\mathrm{pr}}$ flops ($2N_{\mathrm{pr}}$ real multiplications and additions each). An N_D-length output vector (to represent D) needs about $\mathrm{PRI}_{\mathrm{out}}/\mathrm{mean}[\mathrm{PRI}_{\mathrm{in}}] \cdot N_D$ input samples. Thus, *each* output sample requires about $4N_{\mathrm{pr}}\mathrm{PRI}_{\mathrm{out}}/\mathrm{mean}[\mathrm{PRI}_{\mathrm{in}}]$ (flops).

BLUI. Here, nonuniformly sampled input SAR data are interpolated, Doppler filtered, and then decimated to produce the uniformly sampled output signal $y(\cdot)$ [9], [10], [31].

Interpolation Stage. To compute the interpolated sample $r(n)$, BLUI uses Q nonuniformly sampled input samples of $s'(\cdot)$ located at $\mathcal{Q}_n \equiv \{n_1, \ldots, n_Q\}$ and falling within the interval $[-L_{\mathrm{RA}}, +L_{\mathrm{RA}}]$ on either side of n. Here, L_{RA} is the real aperture length, V_p (m/s) is the platform velocity, and $Q = \lfloor (2\,L_{\mathrm{RA}}/\mathrm{PRI}_{\mathrm{in}}V_p) \rfloor$. The interpolated value is $r(n) = \mathbf{b}(\mathcal{Q}_n^+)^T \widehat{\mathbf{s}}'(\mathcal{Q}_n)$. Here, $\widehat{\mathbf{s}}'(\mathcal{Q}_n) = [s'(n_1), \ldots, s'(n_Q)]^T \in \mathbb{C}^{Q\times 1}$ is the input data value 'segment' and $\mathbf{b}(\mathcal{Q}_n^+) = \mathbf{G}(\mathcal{Q}_n)^{-1}\boldsymbol{\varrho}(\mathcal{Q}_n^+) \in \mathbb{R}^{Q\times 1}$, where $\mathbf{G}(\mathcal{Q}_n) \in \mathbb{R}^{Q\times Q}$ is a symmetric matrix (with equal diagonal entries) and $\boldsymbol{\varrho}(\mathcal{Q}_n^+) \in \mathbb{R}^{Q\times 1}$ is a function of both n and $\mathcal{Q}(n)$, i.e., $\mathcal{Q}_n^+ = \{n, \mathcal{Q}(n)\}$.

Filtering and Decimation Stages. Interpolated data $r(\cdot)$ are Doppler filtered using a N_{BLUI}-tap filter with $N_{\mathrm{BLUI}} = 25$ or 17. A nine-tap low-order Capon beamformer provides acceptable passband, but introduces significant passband attenuation requiring additional compensation during processing [31].

Joint BLUI. To avoid the heavy a computational burden imposed by the above three-stage implementation, a *joint BLUI scheme* wherein the matrix operations are carried out on-ground and the three stages are jointly conducted on-board is suggested in [9] and [10], without further details of such a scheme.

To compare the computational complexities, we now develop this joint BLUI scheme. Note that $r(\cdot)$ is first sent through an order-N_{BLUI} digital filter with coefficient vector $\mathbf{h} = [h_0, \ldots, h_{N_{\mathrm{BLUI}}}]^T$ and then decimated by L_{BLUI} to get

$$y(n) = \sum_{k=0}^{N_{\mathrm{BLUI}}} h_k\, r(n'-k) = \sum_{k=0}^{N_{\mathrm{BLUI}}} h_k\, \mathbf{b}\big(\mathcal{Q}_{n'-k}^+\big)^T \widehat{\mathbf{s}}'(\mathcal{Q}_{n'-k}) \tag{17}$$

where, for notational convenience, we use $n' = nL_{\mathrm{BLUI}}$.

1) Arbitrary Input PRF Variation: Entries of $\widehat{\mathbf{s}}'(\cdot)$, $\mathbf{G}(\cdot)$, $\boldsymbol{\varrho}(\cdot)$, and hence $\mathbf{b}(\cdot)$ are functions of $\mathcal{Q}_n$ and the location n. Thus, one must freshly generate $\mathbf{G}(\mathcal{Q}_{n'})$, $\boldsymbol{\varrho}(\mathcal{Q}_{n'}^+)$, and $\mathbf{b}(\mathcal{Q}_{n'}^+)$ on-ground, and uplink the latter, for *each* n. Regarding on-ground computations, $\boldsymbol{\varrho}(\mathcal{Q}_{n'}^+)$ and $\mathbf{G}(\mathcal{Q}_{n'})$ require $\mathrm{F}_R\, Q$ (flops) and $\mathrm{F}_R\,(Q^2 - Q + 2)/2$ (flops), respectively, where F_R is the flop count for computing each entry of the input azimuth signal's autocorrelation function $R_u(\xi)$ [9]; and $\mathbf{b}(\mathcal{Q}_{n'}^+) = \mathbf{G}(n)^{-1}\boldsymbol{\varrho}(n)$ requires $2Q^3/3 + 3Q^2/2 - 7Q/6$ (flops) with Gaussian elimination (and backward substitution) [29], [32]. Regarding on-board computing of $y(n)$, computing $r(n' - k)$, multiplying by h_k, and then adding the $N_{\mathrm{BLUI}}+1$ terms in (17) require $4Q(N_{\mathrm{BLUI}} + 1) - 1$ (flops).

The flop counts for the synthetic data cases in [9] (the fast PRI case is identical to the slow PRI case) appear in Table V. Clearly, the POLYPHASE offers a significant computational advantage.

2) Periodic Input PRF Variation: Suppose, as in staggered SAR, the input PRI sequence repeats every T_{PRI}(s), or every N_{PRI} samples. Then, suppose an integer number R of (predecimation) output samples 'fit' within T_{PRI}(s), i.e., $R \equiv L_{\mathrm{BLUI}} T_{\mathrm{PRI}}/\mathrm{PRI}_{\mathrm{out}} \in \mathbb{N}_+$. Then, BLUI could be made computationally very efficient because $\mathcal{Q}_n$, and therefore $\mathbf{G}(\mathcal{Q}_n)^{-1}$, $\boldsymbol{\varrho}(\mathcal{Q}_n^+)$, and $\mathbf{b}(\mathcal{Q}_n^+)$, also repeat every R samples. In staggered SAR [10], $T_{\mathrm{PRI}} = N_{\mathrm{PRI}}\mathrm{mean}[\mathrm{PRI}_{\mathrm{in}}]$ so that

$$R = L_{\mathrm{BLUI}} N_{\mathrm{PRI}} \mathrm{mean}[\mathrm{PRI}_{\mathrm{in}}]/\mathrm{PRI}_{\mathrm{out}} \in \mathbb{N}_+. \tag{18}$$

The work [10] in fact satisfies (18) with $L_{\mathrm{BLUI}} = 3$ and $\{\mathrm{mean}[\mathrm{PRI}_{\mathrm{in}}], \mathrm{PRI}_{\mathrm{out}}\} = \{0.37037, 1.11111\}$. But, this is not true with the input PRI variations in Fig. 6 when the parameters in [9] are used. To exploit joint BLUI's computational advantage, one may select, for example, $\mathrm{PRI}_{\mathrm{out}} = 0.770$ (ms) (instead of $\mathrm{PRI}_{\mathrm{out}} = 0.417$ ms used in [9]).

When (18) is satisfied, instead of (17), we may use

$$y(n) = \sum_{k=0}^{N_{\mathrm{BLUI}}} h_k\, \mathbf{b}\big(\mathcal{Q}_{n'-k}^+\big)_R^T \widehat{\mathbf{s}}'(\mathcal{Q}_{n'-k}) \tag{19}$$

where $(\cdot)_R$ denotes the modulo-R operation. Thus, the entries of $\mathbf{b}(\cdot)$ are reusable and only R of its samples need be computed.

Moreover, an overlap between consecutive segments $\widehat{\mathbf{s}}'(\mathcal{Q}_{n'-k})$ and $\widehat{\mathbf{s}}'(\mathcal{Q}_{n'-k+1})$ leads to further computational reduction. For example, suppose the first entry of the segment $\widehat{\mathbf{s}}'(\mathcal{Q}_{n'-N_{\mathrm{BLUI}}})$ is $s'(1)$ and only Ψ samples (where $1 \le \Psi \le Q$) are 'new' between consecutive segments. In fact, an approximate expression for Ψ is

$$\Psi \approx \min\{\lceil \mathrm{PRI}_{\mathrm{out}}/L_{\mathrm{BLUI}}\mathrm{mean}[\mathrm{PRI}_{\mathrm{in}}]\rceil, Q\}. \tag{20}$$

Then, one can show that only $N_{\mathrm{BLUI}}\Psi + Q$ samples of the nonuniformly sampled signal $s'(\cdot)$ are needed to compute one output sample. This allows (19) to be expressed as

$$y(n) = \sum_{m=1}^{N_{\mathrm{BLUI}}\Psi + Q} c_m\, s'(m) \tag{21}$$

for appropriately chosen coefficients c_m. Assuming the coefficients are computed on-ground and uploaded, each output sample would require about $4(N_{\mathrm{BLUI}}\Psi + Q) - 2$ (flops).

When input PRF variation is periodic and (18) holds true, Table V compares the flop counts of the two schemes. BLUI shows a significant improvement when compared with its arbitrary case. However, for the fast PRI and elaborate PRI sequences, POLYPHASE still offers a significant computational advantage in on-board flops; for the staggered system in [10], on-board flop counts are comparable. What must be emphasized here is that POLYPHASE applies to arbitrary PRI variations. Moreover, it requires neither uplinking/downlinking nor on-ground computation of intermediate variables. The computation of $R_u(\xi)$ may require numerical schemes [9], which may further exacerbate the BLUI's on-ground effort. Moreover, since $R_u(\xi) = 0$, $\forall |\xi| \ge L_{\mathrm{RA}}/V_p$ [9], BLUI mandates a lower bound on the minimum real aperture length L_{RA}. POLYPHASE makes no such demands.

B. Computational Considerations

1) Convolution Computation: In our implementation of POLYPHASE, we reindex $y'(n)$ to work with $\tilde{y}'(n) = y'(n + (N_{\mathrm{pr}}+1)/2)$, because the associated inequalities are more symmetric, e.g., corresponding to (16), we get

$$\left\lfloor \frac{\ell - 1}{L} \right\rfloor - \left(\frac{N_{\mathrm{pr}} - 1}{2}\right) \le n \le \left\lfloor \frac{\ell}{L} \right\rfloor + \left(\frac{N_{\mathrm{pr}} - 1}{2}\right). \tag{22}$$

The output vectors $\widetilde{\mathbf{y}}'(N_1{:}N_2) = [\tilde{y}'(N_1), \ldots, \tilde{y}'(N_2)]^T$ are simultaneously and efficiently computed via an *input-centered convolution* scheme [12] (see Algorithm 1).

Algorithm 1 Input-Centered Convolution Algorithm

```
Initialize: ỹ'(N1:N2) = 0;
for r(ℓ) ≠ 0, s.t. ℓ ∈ ℕ satisfies (23), do
  m = ⌊(ℓ − 1)/L⌋ + 1;
  for n ∈ ℕ, s.t. n satisfies (22), do
    ỹ'(n) = ỹ'(n) + f_{mL−ℓ}(n + (N_pr + 1)/2 − m) r(ℓ);
  end for
end for
```

Note that the computation of $\widetilde{\mathbf{y}}'(N_1{:}N_2)$ requires all the nonzero input samples $r(\ell) \neq 0$, $\ell \in \mathbb{N}$, such that

$$\left(N_1 - \frac{N_{\mathrm{pr}} - 1}{2}\right) L \le \ell \le \left(N_2 + \frac{N_{\mathrm{pr}} + 1}{2}\right) L. \tag{23}$$

The output $\widetilde{\mathbf{y}}'(N_1{:}N_2)$ from Algorithm 1 yields $\mathbf{y}'(N_1 + (N_{\mathrm{pr}} + 1)/2{:}N_2 + (N_{\mathrm{pr}} + 1)/2)$. Grid alignment (see Section IV-B) can be incorporated directly into this computation instead of accounting for it earlier. Indeed, the computation is carried out 'on-the-fly' with no need to buffer the input signal pulses: the implementation waits for a new nonzero signal pulse $s'(k) = s(\nu_r, \alpha_k)$, generates $r(n)$ in (8), and invokes Algorithm 1.

2) Buffer Memory: The implementation occurs in-place requiring a buffer of size N_D complex floats to store the output, a buffer of $(N_{\mathrm{pr}}L + 1)$ real floats to store the filter coefficients, and one complex float to store the current input temporarily for processing (and later overwrite it with the next input).

Since $N_D = (N_{\mathrm{FFT}}/p_d)\, K_{\mathrm{cr}}$ [see (7)], the parameters N_{FFT}, p_d, and/or K_{cr} can be used to significantly lower the number of output pulses. However, lowering the FFT size

TABLE V
NUMBER OF FLOPS REQUIRED TO COMPUTE (ON A *Per-Output* BASIS)

Scheme	Operation	Flop Count Estimate	Fast PRI Variation in [9]	Elaborate PRI Variation in [9]	Staggered System in [10]
Common Parameters	BLUI: $L_{\text{RA}} = 10$ (m), $L_{\text{BLUI}} = 3$, $N_{\text{BLUI}} = 9$, $V_p = 7,473$ (m/s), $\text{F}_R \approx 24$; POLYPHASE: $N_{pr} = 5$.				
Other Parameters	PRI_{in} (ms)		$[0.349, 0.421]$	$[0.309, 0.461]$	—
	Q		$6\sim7$	$5\sim8$	$5\sim8$
	mean$[PRI_{in}]$ (ms)		0.385	0.385	0.37037
BLUI (Arbitrary)	PRI_{out} (ms)		(a) 0.417	(a) 0.417	
	Up/Down-link floats	$2Q$	$12\sim14$	$10\sim16$	
	ON-BOARD flops	$4Q(N_{\text{BLUI}}+1) + 2N_{BLUI}$	$\mathbf{258\sim298}$	$\mathbf{218\sim338}$	
	On-ground flops	$2Q^3/3 + Q^2(\text{F}_R+3)/2 + Q(\text{F}_R-7/3)/2 + \text{F}_R$	$\mathbf{719\sim990}$	$\mathbf{499\sim1,316}$	
BLUI (Periodic)	PRI_{out} (ms)		(b) 0.770	(b) 0.770	1.11111
	Ψ (from (20))		1	1	1
	Up/Down-link floats	$N_{BLUI}\Psi + Q$	$15\sim16$	$14\sim17$	$14\sim17$
	ON-BOARD flops	$4(N_{BLUI}\Psi+Q) - 2$	$\mathbf{58\sim62}$	$\mathbf{54\sim66}$	$\mathbf{54\sim66}$
	On-ground flops	Same as for arbitrary case; but computed only R times			
POLYPHASE (Arbitrary, including Periodic)	**ON-BOARD flops**	$4N_{pr}PRI_{\text{out}}/\text{mean}[PRI_{\text{in}}]$	$\mathbf{22}$	$\mathbf{22}$	$\mathbf{60}$

(a) We use $PRI_{out} = 0.417$ (ms) because the performance comparison in Section VI-A is conducted with the same value.
(b) $PRI_{out} = 0.770$ (ms) is used so that (18) is satisfied and the computational simplification of the BLUI periodic case can be harnessed.

narrows the unambiguously sampled cross-range extent being imaged; lowering K_{cr} broadens the resolution; and increasing p_d increases the spectrum oversampling factor.

3) Real-Time Application: POLYPHASE executes in real time, i.e., it processes the input pulses one-by-one as they are received with no delay. It handles input pulses even if they are received out of order (assuming they are spatially correctly stamped of course). BLUI does not possess this feature.

4) Data Uplink/Downlink: With its significantly lower computational burden, *all* processing in POLYPHASE can be performed on-board with no need for on-ground computations or uplinking/downlinking of intermediate variables. These translate into lower transmit power (an important consideration when using drones or other UAVs), cheaper and lighter communication systems with smaller channel capacities, and faster data transfers with reduced need for retransmission [33].

5) Error Analysis: Considering the floor operation associated with the grid alignment process in (8), we may upper bound the error in sample realignment by

$$\Delta u_{\text{error}} \leq \frac{\Delta u_{\text{out}}}{L} = \frac{1}{L}\frac{D}{N_D} = \frac{D}{L}\frac{p_d}{N_{\text{FFT}}}\frac{1}{K_{\text{cr}}}. \tag{24}$$

Thus, Δu_{error} can be significantly reduced using larger N_{FFT}, which increases the computational load in SAR processing, or larger L, which calls for a larger number of subfilters. But POLYPHASE's computational load remains unaltered because it is a function of N_{pr} (and not L). Of course, a larger L may produce a better interpolation and hence a better output.

C. Other Design Considerations

1) FFT Size: While it is common to select the FFT size for azimuth compression to accommodate a required cross-range extent, we employed a different strategy: we first selected an FFT size N_{FFT} that can be comfortably implemented with the given system resources and used the cross-range extent X_{out}, which can be accommodated with this N_{FFT} value (see Section IV). This strategy allows one to partition an image into smaller patches and still operate on the same FFT size.

2) Prototype Digital Filter: Given the cross-range extent associated with the selected FFT size, the FIR prototype filter was designed to pass only a portion (we used $\gamma = N_{\text{save}}/N_{\text{FFT}} = \text{PBW}/\text{PRF}_{\text{out}} = 2/3$) of the spectrum (see Fig. 2). This was necessary to arrive at a low-order filter design.

3) Type of Digital Filter: An FIR digital filter of low order ($N_{\text{pr}} = 5$) was adequate for our purposes. In addition to the absence of stability issues, the FIR design allowed us to compute only every Lth output sample that is affected by an incoming input sample. This property was critical for implementing the downsampling portion of our system.

4) Oversampling of Final Image: Oversampling the final image generated a final image that was more pleasing to the eyes. We used an oversampling factor of $p_d = 1.5$ to describe each square radar resolution cell of $\delta_r \times \delta_{\text{cr}}$.

5) Missing Samples Case: To compare the performance when additional samples are missing (due to simultaneous Tx/Rx events) in staggered SAR, we randomly removed 10% of the samples from each PRI sequence in Fig. 6 (see Table VI).

1) *ISLR*: POLYPHASE consistently outperforms the BLUI by at least 1.5 dB when samples are missing; the performance difference is much closer when samples are not missing.
2) *PSLR*: BLUI was better with the elaborate PRI sequence.

6) Other Benefits: One potential use of POLYPHASE is to account for different PRFs across different acquisitions in repeat-pass InSAR, a challenge that has been identified in the spotlight (SL), high-resolution spotlight (HS), and the recent staring spotlight SAR modes of TerraSAR-X. These modes may not be able to collect data from the same scene at the same PRF [36], which poses a significant challenge in interferometry. POLYPHASE can be employed to unify the different PRFs across different SLCs, so that interferometry

TABLE VI
COMPARISON WHEN 10% OF SAMPLES ARE MISSING

Reference	BLUI			POLYPHASE		
(Constant)	Slow	Fast	More Elaborate	Slow	Fast	More Elaborate
ISLR (dB): [34]						
−18.26	−16.11	−16.08	−16.07	−17.61	−17.89	−17.85
ISLR (dB): [35]						
−20.51	−17.13	−17.09	−17.07	−20.43	−20.43	−20.44
PSLR (dB):						
−32.18	−29.02	−28.91	−28.93	−31.09	−31.19	−27.25

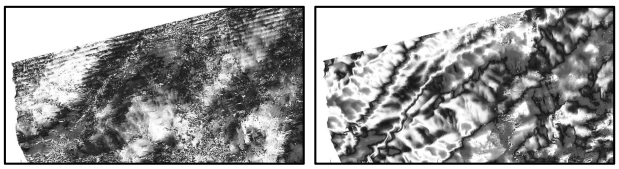

(a) (b)

Fig. 12. Georeferenced interferograms of TerraSAR-X HS mode formed with SLCs. The phase has been wrapped to be within $[-\pi, +\pi]$. (a) Different PRFs {8300; 8200}. (b) Same PRFs {8300; 8300}.

can be applied with equivalent spectrum widths. Fig. 12(a) shows the effect of this phenomenon on real data from TerraSAR-X spotlight interferometry; Fig. 12(b) shows the absence of this effect when the same PRF is used.

The popular solution to unify different SLCs to a common grid space and Doppler spectrum width is to undertake coregistration in two steps.

1) Resample the slave image in the image domain to the geometry of the master image information and low-resolution digital elevation model.
2) Estimate the residual shifts in range and azimuth within subpixel accuracy via point-like scatterers that are common to both images [37]. The success of this strategy depends on a high persistence of the scatterers. Step 2 becomes more challenging at higher resolutions when cells smaller than 1 m are needed for subpixel accuracy. POLYPHASE resolves this issue directly without the need for such meticulous coregistration techniques.

More importantly, POLYPHASE can be used when the PRI sequence may not be periodic and the effects of nonuniform sampling across the aperture have to be compensated for, e.g., missing data, flight path deviation, imaging while in turn, and acceleration and deceleration. A case in point is dual-aperture SAR processing. Traditionally, coherent change detection (CCD) and ground moving target indicator (GMTI) algorithms, both of which are based on dual-aperture SAR processing algorithms, remove clutter by subtracting the SAR images formed within each aperture [38]. If the sampling rates are not uniform across apertures, the performance of clutter cancellation algorithms can be significantly diminished [39]. POLYPHASE offers an effective solution because it does not assume any periodicity condition on the PRI sequence.

VIII. CONCLUSION

POLYPHASE is a computationally efficient method for resampling along-track oversampled SAR data in slow-time domain for a radar that operates at variable PRFs. We provide a lower bound on the sparseness of the received SAR data relative to the output grid, which ensures that the uniformly resampled data approximate the spectral properties of a decimated version of a certain hidden densely sampled SAR data sequence. In essence, we view the nonuniformly spaced received samples as a subset of samples of a uniformly densely sampled underlying signal. A low-pass filter, implemented via its polyphase components, generates the missing sample values. Only the portion of interest from the spectrum is extracted in the frequency domain after taking the spatial azimuth compression FFT. The order of each polyphase subfilter and the polyphase implementation are critical factors affecting the computational complexity of the algorithm.

When compared with BLUI in [9], POLYPHASE provides significant savings in computational cost without sacrificing performance. It can be implemented in real time and completely on-board with no downlinking of intermediate variables for on-ground computations. It can even accommodate out-of-order input samples. POLYPHASE can also be useful in other application scenarios, e.g., it can be employed to unify PRFs across a sequence of repeat-pass acquisitions taken at different PRFs in TerraSAR-X spotlight mode data and to improve clutter cancellation in CCD and GMTI.

APPENDIX A
ANALYTICAL BASIS OF THE RESAMPLING SCHEME

As argued in Sections III-B and IV-B, we model the signal $r(n)$ in Fig. 1 as $r(n) = g(n)\,s(n)$. Here, the gating function $g(n)$ is a realization of the i.i.d. Bernoulli random process with parameter p in (3). Thus, $r(n) = s(n)$ whenever $g(n) = 1$, and $r(n) = 0$ [i.e., $r(n)$ is 'missing' a sample of $s(n)$] otherwise. The mean of the w.s.s. random process $g(\cdot)$ is $\mu_g = p$, $\forall n \in \mathbb{N}$; its autocorrelation $C_g(n) = p(1-p)\,\delta(n) + p^2$ and PSD $S_g(\omega)$ form a DT FT pair so that

$$S_g(\omega) = p(1-p) + (2\pi p^2) \sum_{k=-\infty}^{+\infty} \delta_D(\omega - 2\pi k). \quad (25)$$

With $f(n)$ being the IPR of the digital filter $F(z)$, we have

$$\begin{aligned} r(n) &= g(n)\,s(n); \quad v(n) = f(n) * r(n) \\ v(n) &= (f(n) * g(n))\,v'(n). \end{aligned} \quad (26)$$

Note that $f(n) \leftrightarrow F(\omega)$. Thus

$$y(n) = v'(nL) = (f(n) * r(n))/(f(n) * g(n))|_{n \to nL}. \quad (27)$$

In terms of PSDs, we can express (26) as

$$S_r(\omega) = \frac{1}{2\pi}\,(S_g(\omega) * S_s(\omega)); \quad S_v(\omega) = |F(\omega)|^2 S_r(\omega). \quad (28)$$

The normalization step in (26) and (27) can be expressed as

$$\begin{aligned} S_v(\omega) &= \frac{1}{2\pi}\,((|F(\omega)|^2 S_g(\omega)) * S_{v'}(\omega)) \\ S_y(\omega) &= \frac{1}{L}\sum_{\ell=0}^{L-1} S_{v'}(\omega_\ell), \quad \omega_\ell = \frac{\omega}{L} - \frac{2\pi\ell}{L}. \end{aligned} \quad (29)$$

Take the expressions for $S_v(\omega)$ in (28) and (29) and use (25) to substitute for $S_g(\omega)$

$$\begin{aligned} S_v(\omega) &= p\,|F(\omega)|^2 \left[\frac{(1-p)}{2\pi}\int_\theta S_s(\omega-\theta)\,d\theta + p\,S_s(\omega)\right] \\ &= \frac{p(1-p)}{2\pi}\int_\theta |F(\theta)|^2 S_{v'}(\omega-\theta)\,d\theta \\ &\quad + p^2|F(0)|^2 S_{v'}(\omega). \end{aligned} \tag{30}$$

Claim 1: If $|F(\omega)|$ has support $[-\pi/L, +\pi/L]$, $L \gg 1$, and (6) is true, then the PSD of the output $y(n)$ approximates the PSD of an L-fold decimated version of the densely sampled input signal $s(n)$ in $|\omega| \leq \gamma\,\pi$ when $p \gg \rho/(L+\rho)$. □

Proof: With $L \gg 1$, we note that

$$\int_\theta |F(\theta)|^2 S_{v'}(\omega-\theta)\,d\theta \leq \int_{\theta=-\pi/L}^{+\pi/L} S_{v'}(\omega-\theta)\,d\theta$$

which can be approximated by $(2\pi/L)\,S_{v'}(\omega)$. In the second equation in (30), the first term is much smaller than the second term if $p \gg 1/(L+1)$. Then (30) becomes

$$\begin{aligned} S_v(\omega) &= p\,|F(\omega)|^2 \left[\frac{(1-p)}{2\pi}\int_\theta S_s(\omega-\theta)\,d\theta + p\,S_s(\omega)\right] \\ &\approx \frac{2\pi p^2}{2\pi}\,S_{v'}(\omega). \end{aligned}$$

Now, use the expression for $S_y(\omega)$ in (29) to get

$$\begin{aligned} \frac{1}{L}\sum_{\ell=0}^{L-1} S_v(\omega_\ell) &= \frac{p(1-p)}{2\pi L}\sum_{\ell=0}^{L-1}|F(\omega_\ell)|^2\int_\theta S_s(\omega_\ell-\theta/L)\,d\theta \\ &\quad + \frac{2\pi p^2}{2\pi L}\sum_{\ell=0}^{L-1}|F(\omega_\ell)|^2 S_s(\omega_\ell) \qquad (31) \\ &\approx \frac{2\pi p^2}{2\pi L}\sum_{\ell=0}^{L-1} S_{v'}(\omega_\ell) = \frac{2\pi p^2}{2\pi}\,S_y(\omega). \qquad (32) \end{aligned}$$

Consider (31): $|F(\omega_\ell)| = 1$, $|\omega| \leq \gamma\,\pi$, and $S_s(\omega)$ has the support $[-\rho\pi/L, +\rho\pi/L]$, where $\rho \geq 1$. Thus

$$\int_\theta S_s(\omega_\ell-\theta/L)\,d\theta \approx (2\rho\pi/L)\,S_s(\omega_\ell). \tag{33}$$

Thus, for $|\omega| \leq \gamma\,\pi$, we may approximate (31) as

$$\frac{1}{L}\sum_{\ell=0}^{L-1} S_v(\omega_\ell) \approx \frac{2\pi p^2}{2\pi L}\sum_{\ell=0}^{L-1} S_s(\omega_\ell), \text{ for } p \gg \rho/(L+\rho).$$

Use this instead of (31) to express (31) and (32) as

$$\frac{1}{L}\sum_{\ell=0}^{L-1} S_v(\omega_\ell) \approx \frac{2\pi p^2}{2\pi L}\sum_{\ell=0}^{L-1} S_s(\omega_\ell) \approx \frac{2\pi p^2}{2\pi}\,S_y(\omega). \qquad ■$$

APPENDIX B
OPERATION OF THE POLYPHASE COMPONENTS

Claim 2: Consider a nonzero input sample $r(\ell^*) \neq 0$ such that $\ell^* \in \mathbb{N}$ and $(n - N_{\text{pr}})L \leq \ell^* \leq nL$. The only polyphase component that operates on $r(\ell^*)$ is $f_x(\cdot)$, where $x = m^*L - \ell^*$, with

$$m^* = \left\lfloor \frac{\ell^*-1}{L} \right\rfloor + 1 \implies x = (L-\ell^*) + L\left\lfloor \frac{\ell^*-1}{L} \right\rfloor. \quad □$$

Proof: First, suppose $(n - N_{\text{pr}})L + 1 \leq \ell^* \leq nL$ that corresponds to the summation term in (15). The polyphase components that operate on $r(\ell^*)$ are $f_x(\cdot)$, where $x = m^*L - \ell^* \in \overline{0, L-1}$ with $m^* \in \overline{n - N_{\text{pr}} + 1, n}$. But $m^*L - \ell^* = x$ iff $(m^*-1)L + (L-1-x) = \ell^* - 1$. Since $(L-1-x) \in \overline{0, L-1}$, we conclude that $L-1-x = (\ell^*-1)_L$. This yields $x = (L-1) - (\ell^*-1)_L = (L-\ell^*) + L\lfloor(\ell^*-1)/L\rfloor$. The claim then follows for $(n - N_{\text{pr}})L + 1 \leq \ell^* \leq nL$.

Next, suppose $\ell^* = (n - N_{\text{pr}})L$ that corresponds to the first term in (15), namely, $f_0(N_{\text{pr}})\,r((n - N_{\text{pr}})L)$. When $\ell^* = (n - N_{\text{pr}})L$ is substituted in the claimed expressions for x and m^*, we get $x = 0$ and $m^* = n_{\text{pr}}$, which are consistent with $f_0(N_{\text{pr}})\,r((n - N_{\text{pr}})L)$.

REFERENCES

[1] A. Moreira, P. Prats-Iraola, M. Younis, G. Krieger, I. Hajnsek, and K. P. Papathanassiou, "A tutorial on synthetic aperture radar," *IEEE Geosci. Remote Sens. Mag.*, vol. 1, no. 1, pp. 6–43, Mar. 2013.

[2] G. Krieger, N. Gebert, and A. Moreira, "SAR signal reconstruction from non-uniform displaced phase centre sampling," in *Proc. IEEE Int. Geosci. Remote Sens. Symp. (IGARSS)*, vol. 3. Anchorage, AK, USA, Sep. 2004, pp. 1763–1766.

[3] N. Gebert, G. Krieger, and A. Moreira, "SAR signal reconstruction from non-uniform displaced phase center sampling in the presence of perturbations," in *Proc. IEEE Int. Geosci. Remote Sens. Symp. (IGARSS)*, vol. 2. Seoul, South Korea, Jul. 2005, pp. 1034–1037.

[4] N. Gebert, G. Krieger, and A. Moreira, "Multichannel azimuth processing in ScanSAR and TOPS mode operation," *IEEE Trans. Geosci. Remote Sens.*, vol. 48, no. 7, pp. 2994–3008, Jul. 2010.

[5] Y. Jiang, X. Wu, and B.-B. Zhang, "Study on spectrum reconstruction algorithm for high resolution and wide swath space-borne SAR," in *Proc. Int. Symp. Instrum. Meas., Sens. Netw. Autom. (IMSNA)*, vol. 1. Sanya, China, Aug. 2012, pp. 200–204.

[6] G. H. Goldman, "Computationally efficient resampling of nonuniform oversampled SAR data," in *Proc. IEEE Radar Conf.*, Washington, DC, USA, May 2010, pp. 70–74.

[7] J. L. Walker, "Range-Doppler imaging of rotating objects," *IEEE Trans. Aerosp. Electron. Syst.*, vol. 16, no. 1, pp. 23–52, Jan. 1980.

[8] M. Soumeck, *Fourier Array Imaging*. Englewood Cliffs, NJ, USA: Prentice-Hall, 1994.

[9] M. Villano, G. Krieger, and A. Moreira, "Staggered SAR: High-resolution wide-swath imaging by continuous PRI variation," *IEEE Trans. Geosci. Remote Sens.*, vol. 52, no. 7, pp. 4462–4479, Jul. 2014.

[10] M. Villano, G. Krieger, and A. Moreira, "Data volume reduction in high-resolution wide-swath SAR systems," in *Proc. Asia–Pacific Conf. Synth. Aperture Radar (APSAR)*, Singapore, Sep. 2015, pp. 119–124.

[11] D. R. Wehner, *High Resolution Radar*. Norwood, MA, USA: Artech House, 1987.

[12] W. G. Carrara, R. S. Goodman, and R. M. Majewski, *Spotlight Synthetic Aperture Radar: Signal Processing Algorithms*. Boston, MA, USA: Artech House, 1995.

[13] C. V. Jakowatz, Jr., D. E. Wahl, P. H. Eichel, D. C. Ghiglia, and P. A. Thompson, *Spotlight-Mode Synthetic Aperture Radar: A Signal Processing Approach*. New York, NY, USA: Springer, 1996.

[14] M. Soumeck, *Synthetic Aperture Radar Signal Processing With MATLAB Algorithms*. Hoboken, NJ, USA: Wiley, 1999.

[15] N. Gebert and G. Krieger, "Ultra-wide swath SAR imaging with continuous PRF variation," in *Proc. Eur. Conf. Synth. Aperture Radar (EUSAR)*, Aachen, Germany, Jun. 2010, pp. 1–4.

[16] L. Yadong and C. Qian, "A novel ultra-wide swath SAR based on variable PRF and digital beamforming," in *Proc. IET Int. Radar Conf.*, Xi'an, China, Apr. 2013, pp. 1–5.

[17] X. Luo, R. Wang, W. Xu, Y. Deng, and L. Guo, "Modification of multichannel reconstruction algorithm on the SAR with linear variation of PRI," *IEEE J. Sel. Topics Appl. Earth Observ. Remote Sens.*, vol. 7, no. 7, pp. 3050–3059, Jul. 2014.

[18] A. V. Oppenheim and R. Schafer, *Digital Signal Processing*. Englewood Cliffs, NJ, USA: Prentice-Hall, 1975.

[19] R. E. Crochiere and L. R. Rabiner, "Interpolation and decimation of digital signals—A tutorial review," *Proc. IEEE*, vol. 69, no. 3, pp. 300–331, Mar. 1981.

[20] T. Saramaki, Y. Neuvo, and S. K. Mitra, "Design of computationally efficient interpolated FIR filters," *IEEE Trans. Circuits Syst.*, vol. 35, no. 1, pp. 70–88, Jan. 1988.

[21] R. Lyons, "Interpolated narrowband lowpass FIR filters," *IEEE Signal Process. Mag.*, vol. 20, no. 1, pp. 50–57, Jan. 2013.

[22] T. W. Parks and C. S. Burrus, "Digital filter design," *Topics in Digital Signal Processing*. New York, NY, USA: Wiley, 1987.

[23] T. I. Laakso, V. Valimaki, M. Karjalainen, and U. K. Laine, "Splitting the unit delay," *IEEE Signal Process. Mag.*, vol. 13, no. 1, pp. 30–60, Jan. 1996.

[24] H. Knutsson and C.-F. Westin, "Normalized and differential convolution," in *Proc. IEEE Comput. Soc. Conf. Comput. Vis. Pattern Recognit. (CVPR)*, New York, NY, USA, Jun. 1993, pp. 515–523.

[25] C.-F. Westin, K. Nordberg, and H. Knutsson, "On the equivalence of normalized convolution and normalized differential convolution," in *Proc. IEEE Int. Conf. Acoust., Speech, Signal Process. (ICASSP)*, vol. 5. Adelaide, SA, Australia, Apr. 1994, pp. V/457–V/460.

[26] K. Andersson and H. Knutsson, "Continuous normalized convolution," in *Proc. IEEE Int. Conf. Multimedia Expo (ICME)*, vol. 1. Lausanne, Switzerland, Aug. 2002, pp. 725–728.

[27] S. Barbarossa, "Detection and imaging of moving objects with synthetic aperture radar. 1. Optimal detection and parameter estimation theory," *IEE Proc. F, Radar Signal Process.*, vol. 139, no. 1, pp. 79–88, Feb. 1992.

[28] J. Russ, *The Image Processing Handbook*. Boca Raton, FL, USA: CRC Press, 2011.

[29] O. Axelsson, *Iterative Solution Methods*. Cambridge, U.K.: Cambridge Univ. Press, 1996.

[30] S. G. Johnson and M. Frigo, "A modified split-radix FFT with fewer arithmetic operations," *IEEE Trans. Signal Process.*, vol. 55, no. 1, pp. 111–119, Jan. 2007.

[31] M. Villano, G. Krieger, and V. D. Zoppo, "On-board doppler filtering for data volume reduction in spaceborne SAR systems," in *Proc. 15th Int. Radar Symp. (IRS)*, Gdańsk, Poland, Jun. 2014, pp. 1–6.

[32] J. R. Bunch and B. N. Parlett, "Direct methods for solving symmetric indefinite systems of linear equations," *SIAM J. Numer. Anal.*, vol. 8, no. 4, pp. 639–655, Dec. 1971.

[33] J. G. Proakis, *Digital Communications*. New York, NY, USA: McGraw-Hill, 2001.

[34] S. Holm, P. A. Valand, and K. Eldhuset, "Performance of Cesar ERS-1 SAR processor," in *Proc. IEEE Int. Geosci. Remote Sens. Symp. (IGARSS)*, Helsinki, Finland, Jun. 1999, pp. 291–294.

[35] M. P. Zenere, "SAR image quality assessment," Master Emergency Early Warning Response Space Appl., Univ. Nacional Córdoba, Córdoba, Argentina, Tech. Rep., Mar. 2012. [Online]. Available: https://pdfs.semanticscholar.org/13de/c8c31f0d79fac42191f3f5e4dbddfb3de790.pdf

[36] M. Eineder, N. Adam, R. Bamler, N. Yague-Martinez, and H. Breit, "Spaceborne spotlight SAR interferometry with TerraSAR-X," *IEEE Trans. Geosci. Remote Sens.*, vol. 47, no. 5, pp. 1524–1535, May 2009.

[37] N. Adam, B. Kampes, M. Eineder, J. Worawattanamateekul, and M. Kircher, "The development of a scientific permanent scatterer system," in *Proc. ISPRS/EARSeL Joint Workshop High-Resolution Mapping From Space*, Hannover, Germany, 2003, pp. 1–6.

[38] M. Soumekh, "Moving target detection in foliage using along track monopulse synthetic aperture radar imaging," *IEEE Trans. Image Process.*, vol. 6, no. 8, pp. 1148–1163, Aug. 1997.

[39] M. I. Skolnik, *Introduction to Radar Systems*. New York, NY, USA: McGraw-Hill, 1980.

Yoangel Torres (S'04) received the B.Sc. degree in electrical engineering from Florida State University, Tallahassee, FL, USA, in 2005, and the M.S. degree in electrical engineering from the University of Florida, Gainesville, FL, USA, in 2009. He is currently pursuing the Ph.D. degree with the Department of Electrical and Computer Engineering, University of Miami, Coral Gables, FL, USA.

He is currently a Radar Systems Engineer with Northrop Grumman Corporation, Melbourne, FL, USA, which supports his Ph.D. studies. His research interests include radar systems design, radar mode development, signal processing, and SAR/InSAR systems and their application in tunnel detection.

Kamal Premaratne (SM'94) received the B.Sc. (Hons.) degree in electronics and telecommunication engineering from the University of Moratuwa, Moratuwa, Sri Lanka, in 1982, and the M.S. and Ph.D. degrees in electrical and computer engineering from the University of Miami, Coral Gables, FL, USA, in 1984 and 1988, respectively.

He is currently a Victor P. Clarke Professor with the University of Miami. His research interests include Dempster–Shafer belief theory, evidence fusion, machine learning and knowledge discovery from imperfect data, and opinion and consensus dynamics in social networks.

Dr. Premaratne is a Fellow of IET (formerly IEE). He was a recipient of the Mather Premium from 1992 to 1993 and the Heaviside Premium from 1999 to 2000 from the Institution of Electrical Engineers, London, U.K., and the Eliahu I. Jury Excellence in Research Award in 1991, 1994, and 2001, and the Johnson A. Edosomwan Researcher of the Year Award from the College of Engineering, University of Miami in 2014. He has served as an Associate Editor of the IEEE TRANSACTIONS ON SIGNAL PROCESSING from 1994 to 1996 and the *Journal of the Franklin Institute* from 1993 to 2005.

Falk Amelung received the M.S. degree in geophysics from the University of Münster, Münster, Germany, in 1992, and the Ph.D. degree from the University of Strasbourg, Strasbourg, France, in 1996.

He was with Stanford University, Stanford, CA, USA, and the University of Hawaii, Honolulu, HI, USA. In 2002, he joined the University of Miami, Coral Gables, FL, USA, where he is currently a Professor of Geophysics with the Department of Marine Geosciences, Rosenstiel School of Marine and Atmospheric Science. His research interests include the synthetic aperture radar interferometry (InSAR) study of active volcanism, active tectonics, and land subsidence, and the use of InSAR for volcano monitoring and for measuring subtle tectonic deformation. He is a member of the Science Team of the NASA–ISRO SAR mission.

Shimon Wdowinski received the B.Sc. degree in earth sciences and the M.Sc. degree in geology from Hebrew University, Jerusalem, Israel, in 1983 and 1985, respectively, and the M.S. degree in engineering sciences and the Ph.D. degree in geophysics from Harvard University, Cambridge, MA, USA, in 1987 and 1990, respectively.

He conducted post-doctorate research with the Scripps Institute of Oceanography, University of California, San Diego, CA, USA, from 1990 to 1993. He was an Associate Professor with Tel Aviv University, Tel Aviv-Yafo, Israel, from 1994 to 2004, and a Research Professor with the Rosenstiel School of Marine and Atmospheric Science, University of Miami, Coral Gables, FL, USA, from 2004 to 2016. Since 2016, he has been an Associate Professor with the Department of Earth and Environment, Florida International University, Miami, FL, USA, where he teaches and researches geology and geophysics. His research interests include the development and usage of space geodetic techniques that can detect very precisely small movements of the earth's surface. He successfully applied these technologies to study natural hazards and environmental phenomena, such as earthquakes, land subsidence, and wetland surface flow.